

Local Deformation and Fracture Behavior of High-Strength Aluminum Alloys Under Hydrogen Influence



KAZUYUKI SHIMIZU, HIROYUKI TODA, KENTARO UESUGI,
and AKIHISA TAKEUCHI

The local deformation and fracture behavior of high-Zn Al-Zn-Mg(-Cu) alloys under hydrogen influence were investigated by *in situ* tests through synchrotron X-ray tomography. Intergranular and quasi-cleavage fractures were induced by hydrogen, and strain localization by the presence of cracks was not observed by 3D strain mapping. These results suggest that the strain localization at the crack tip is smaller than the measurement limit of 3D strain mapping. The average crack-tip-opening displacements, which are one of the crack driving forces specified by fracture mechanics, directly measured from the tomographic slice were 0.14 and 0.23 μm for intergranular cracks and quasi-cleavage cracks, respectively. The crack driving forces of the intergranular and quasi-cleavage cracks were small. The local deformation behavior at the crack tips was analyzed based on fracture mechanics. The local deformation field of the crack tip, which was characterized using the Rice–Drugan–Sham (RDS) solution rather than the Hutchinson–Rice–Rosengren (HRR) solution, was located within 20 μm of the crack tip, and its size was limited. The results of this work clarify that the intergranular and quasi-cleavage crack growths are caused by small driving forces; however, this behavior is not perfectly brittle, accompanying local deformation at the crack tip.

<https://doi.org/10.1007/s11661-019-05304-y>

© The Minerals, Metals & Materials Society and ASM International 2019

I. INTRODUCTION

AL-ZN-MG(-CU) alloys are high-strength aluminum alloys that are widely used in aircraft and rolling stock, which require high strength-to-weight ratios. When the Zn or Mg content is increased to improve strength, susceptibility to stress corrosion cracking (SCC) increases, leading to delayed fracture.^[1–3] Therefore, the SCC susceptibility of commercial alloys is suppressed both by adding trace elements such as Cr and Zr and by heat treatments such as overaging and retrogression-and-reaging treatments; the latter is a three-step heat treatment consisting of pre-aging, retrogression, and re-aging.^[4] The SCC of Al-Zn-Mg(-Cu) alloys, particularly for crack growth behavior, has been speculated to be strongly related to hydrogen embrittlement (HE).^[1,5] The SCC and HE of aluminum alloys have been investigated by a slow strain rate test (SSRT).^[6–8] The degradation of mechanical properties

by hydrogen depends on the strain rates in the SSRT. Kuramoto *et al.* reported that the true fracture strain of Al-4.9Zn-2.2Mg-1.3Cu alloy is approximately 17 pct at a strain rate of $1.67 \times 10^{-4} \text{ s}^{-1}$ but decreases to less than 5 pct at a strain rate of $1.67 \times 10^{-7} \text{ s}^{-1}$ in air.^[8] Although SSRT is not employed, the HE of Al-Zn-Mg(-Cu) alloys is observed in tensile tests at strain rates of 10^{-4} to 10^{-3} s^{-1} when the tensile loading is periodically held.^[9] When the holding time is longer, the embrittlement is more prominent. When the holding time increases from 0 to 2.1 ks, the fracture strain decreases from 23 to 10 pct, and the areal fraction of quasi-cleavage fracture increases from 0 to 20 pct. In the SSRT and holding-time tests, the diffusible hydrogen in the material is repartitioned during the plastic deformation, inducing time-dependent fracture.^[10–12] That is, the localization of the hydrogen distribution inside the material strongly influences the mechanical properties in the aforementioned HE experiment.

The hydrogen distribution in a material is not uniform, even without any external stress.^[13] The hydrogen is partitioned into trap sites such as vacancies, solute atoms, dislocations, grain boundaries, particles, and pores.^[14] The hydrogen partitioning in aluminum alloys is modeled as follows:

$$C_H = \theta_L N_L + \sum \theta_i N_i + C_{\text{pore}}, \quad [1]$$

KAZUYUKI SHIMIZU and HIROYUKI TODA are with the Department of Mechanical Engineering, Kyushu University, Motoooka 744, Nishi-ku, Fukuoka-City, Fukuoka, 819-0395, Japan. Contact e-mail: kshimizu@kyudai.jp KENTARO UESUGI and AKIHISA TAKEUCHI are with the Japan Synchrotron Radiation Research Institute, Sayo-gun, Hyogo, 679-5198, Japan.

Manuscript submitted December 28, 2018.

Article published online June 3, 2019

where C_H is the total hydrogen content in a material, and θ_L and θ_i are the occupancies of the interstitial sites and i th trap sites, respectively. N_L and N_i are the trap densities in the normal interstitial lattice sites and i th trap sites, respectively. C_{pore} is the total molecular hydrogen content in the pores. Molecular hydrogen is widely understood to fill micron-sized holes, which are called pores, in aluminum alloys.^[14–17] In aluminum alloys, pores are also present due to the hydrogen solubility gap between the liquid phase and solid phase, even in wrought materials.^[14] It is hypothesized that the pores are filled with molecular hydrogen. The occupancy of hydrogen in each trap site, θ_i , is expressed by Eq. [2] based on Oriani's theory, which describes the local thermal equilibrium between interstitial and other trap sites^[13]:

$$\frac{\theta_i}{1 - \theta_i} = \theta_L \exp\left(\frac{E_b}{RT}\right), \quad [2]$$

where E_b is the binding energy between hydrogen and the i th trap site, R is the gas constant, and T is the temperature. The binding energy is experimentally derived by subtracting the activation energy of hydrogen diffusion in a lattice from the desorption energy measured by thermal desorption analysis (TDA). The binding energies in steel are often evaluated by TDA^[18]; however, such analyses are not straightforward in the case of aluminum alloys^[19,20] because the trap sites of hydrogen easily change with the increasing temperature. Therefore, the binding energy of each type of trap site in aluminum has been investigated by first-principles simulation (FPS), and the energies are 0.02 to 0.19, 0.3, and 0.45 to 0.60 eV at the grain boundaries, vacancies, and surfaces, respectively.^[21] According to Eqs. [1] and [2], the hydrogen partitioned to each trap site increases as the trap-site density and binding energy increase. Unlike the binding energy, the trap-site density readily varies because of the thermal history and deformation.^[2,13,14,20] As the dislocation density increases from 5.36×10^{12} to $2.86 \times 10^{14} \text{ m}^{-2}$ under a 6 pct plastic strain, the trap-site density of the dislocations is estimated to increase from 3.39×10^{22} to $1.81 \times 10^{24} \text{ site/m}^3$.^[20] In general, when plastic strain is applied to a material, the plastic strain (*i.e.*, dislocation) is localized to the grain boundaries, phase boundaries, particles, crack tips, *etc.* under the influences of the microstructure and cracks. Therefore, if hydrogen migrates from other sites or from the environment, the hydrogen content in the dislocations increases, and the hydrogen distribution is expected to localize further. To understand HE from the viewpoint of hydrogen localization, the visualization of the hydrogen distribution in materials is essential. However, hydrogen is the smallest element, and embrittlement occurs on the order of mass ppm. Because direct observation is extremely challenging, hydrogen is indirectly visualized using a hydrogen microprint technique in the many studies on aluminum alloys. The principle of the hydrogen microprint technique is that a silver halide emulsion is coated on the specimen surface, and the hydrogen that migrates from the inside to the surface reduces the silver ions in this

emulsion. The observation of the silver particles thus indirectly enables the visualization of the hydrogen distribution on this surface. Silver particles (corresponding to hydrogen) are detected at the grain boundaries,^[22] particles,^[23,24] slip bands,^[25] and cracks^[26] after plastic deformation, indicating that the hydrogen distribution is localized by loading. The localization of hydrogen and deformations mutually influence each other. Bhuiyan *et al.* reported that the synergistic effect of the tensile stress and high hydrogen content at the crack tip leads to local flow stress reduction and facilitates localized deformation.^[9]

To explain the HE mechanism, frameworks such as the hydrogen-enhanced localized plasticity (HELP), hydrogen-enhanced decohesion (HEDE), and hydrogen-enhanced strain-induced vacancy (HESIV) mechanisms have long been considered.^[27] HELP describes the interaction between dislocations and hydrogen, HEDE describes the reduction of the cohesive bond energy between atoms by hydrogen accumulation, and HESIV describes that hydrogen contributes to the formation of vacancies during deformation. Nevertheless, the discussion continues, and the findings on HE sometimes differ among researchers. First, as a specific example, findings on hydrogen trapping at a grain boundary, which is considered the origin of grain boundary fracture, are described. Yamaguchi *et al.* reported that hydrogen is strongly trapped at a high-angle grain boundary, where the Σ value and the grain boundary energy are high.^[28,29] In addition, Mine *et al.* suggested that high-angle grain boundaries are not effective trap sites but that hydrogen is strongly trapped at low-angle grain boundaries.^[30] Subsequently, Nagumo *et al.* observed that in quasi-cleavage cracks, the excess vacancies stabilized by hydrogen grow into nanovoids and that cracks are initiated by coarsening nanovoids.^[31] Neeraj *et al.* documented the presence of nanodimples on quasi-cleavage facets.^[32] Martin *et al.* concluded that the initiation and the growth of voids along the slip band intersection lead to quasi-cleavage fracture based on transmission electron microscopy (TEM) images of the region just below the quasi-cleavage facet.^[33] Their claims are similar at first sight. However, Neeraj *et al.* concluded that the vacancy-induced nanovoid nucleation and coalescence are a failure mechanism, while Martin *et al.* concluded that plastic processes, which are enhanced and accelerated by the presence of hydrogen, widen voids, producing a fracture surface.

Intergranular and quasi-cleavage cracks constitute well-known HE behavior, but the influences of hydrogen on crack growth and the crack driving forces are not well understood, as mentioned above. Much of the typical evaluation of HE is based on simulations with extremely simplified microstructures or observations after loading/fracture. For a further understanding of HE, it is desirable to observe *in situ* the hydrogen-induced fracture behaviors, *i.e.*, intergranular fracture and quasi-cleavage fracture behaviors, and quantitatively examine them with parameters such as strains and the crack driving forces. To achieve this purpose, 2D observation is insufficient because the stress/strain state is different between the inside and the surface of the

material. The direct observation of the 3D fracture behavior is preferred. The *in situ* observation of the fracture behavior by synchrotron X-ray tomography is suitable for this. In recent years, the spatial resolution of projection-type tomography has reached $1.25\ \mu\text{m}$, approaching the physical limit.^[34] This spatial resolution is enough to observe cracks inside the material. With the 3D strain mapping *via* X-ray tomography developed by Kobayashi *et al.*, it is also possible to analyze the 3D elemental strains inside the material.^[35]

In this study, we experimentally clarify the intergranular/quasi-cleavage fracture behaviors of Al-Zn-Mg (-Cu) alloys under the influence of hydrogen. For this purpose, the elemental strains at the vicinity of the crack tip were directly analyzed by synchrotron X-ray tomography, which enables 3D strain mapping inside a material. Furthermore, the crack morphologies were visualized by imaging-type tomography, developed in recent years, and the crack driving force was analyzed based on the fracture mechanics parameters. In addition, the pores influence the mechanical properties of the aluminum alloys. Toda *et al.* have clarified that the growth and coalescence of pores are the dominant factors leading to the ductile fracture of aluminum alloys.^[17] The origin of the pores is supersaturated hydrogen in the aluminum, and the hydrogen can thus be interpreted as indirectly affecting the mechanical properties through the pores. In this study, both the atomic hydrogen in the matrix and the pores (*i.e.*, molecular hydrogen) were evaluated as factors responsible for the HE.

II. METHODOLOGY

A. Specimens

The materials used in this study were Al-10.1Zn-1.2Mg alloy and modified A7150 alloy. The modified A7150 alloy had a chemical composition (in mass pct) of 9.9 Zn, 2.3 Mg, 1.4 Cu, 0.06 Si, 0.05 Fe, 0.04 Ti, 0.15 Zr, and balance Al (hereinafter, Al-9.9Zn-2.3Mg-1.4Cu alloy). An Al-10.1Zn-1.2 Mg alloy containing trace iron (< 0.01 mass pct Fe) was also prepared. The Al-10.1Zn-1.2Mg alloy was prepared by homogenization at 773 K for 7.2 ks after casting, hot rolling at 723 K with a rolling reduction of 50 pct, and solution treatment at 773 K for 7.2 ks. Immediately after the solution treatment, aging was carried out for 144 ks at 393 K and 25.2 ks at 453 K to overage. The preparation process of the Al-9.9Zn-2.3Mg-1.4Cu alloy was the same as Material MH described in the literature,^[9] and this aging condition was also an overaged one. After aging, all tensile test pieces were processed using wire-cut electrical discharge machining (EDM). The shape of the tensile test pieces is the same as that reported in the literature.^[9,36] The gauge length of the tensile test piece was 0.7 mm, and the cross-sectional area was $0.6 \times 0.6\ \text{mm}^2$. Here, EDM also served as a means of hydrogen charging. Other authors have confirmed that the hydrogen content increases from 0.14 mass ppm to 6.97 mass ppm by EDM in water.^[9,12]

In addition, a high-hydrogen Al-10.1Zn-1.2 Mg alloy was prepared with a hydrogen content higher than the typical hydrogen charge through performing EDM twice on the surface. After EDM, the test piece was considered to have a high hydrogen content on its surface. To distribute the hydrogen to the interior of the specimens, the specimens were stored in acetone for approximately 4 days and subjected to both tomographic experiments and TDA, which is described later. Assuming that the diffusion coefficient of the hydrogen in aluminum at room temperature was $2.1 \times 10^{-13}\ \text{m}^2/\text{s}$,^[37,38] the diffusion distance after 4 days was estimated to be 0.38 mm. This diffusion distance is larger than half of the specimen size, and the hydrogen is thus assumed to diffuse from the surface to the center of the specimens. The aforementioned diffusivity of $2.1 \times 10^{-13}\ \text{m}^2/\text{s}$ was determined by using pure aluminum. The effective diffusivity of the overaged Al-6.9 pct Zn-2.65 pct Mg-0.06 pct Cu alloy has been reported to be $1.05 \times 10^{-11}\ \text{m}^2/\text{s}$ at 298 K.^[39] The diffusion distance after 4 days calculated from this effective diffusivity was 2.7 mm. The diffusion distance calculated from the diffusivity determined for the alloy similar in composition to the one used in this study is sufficiently larger than the specimen size. Therefore, we assumed that hydrogen diffused into the specimen, even if the surface hydrogen concentration slightly changed. In view of this, we speculate that the aforementioned diffusivity of $2.1 \times 10^{-13}\ \text{m}^2/\text{s}$ is conservative.

In addition, four Al-10.1Zn-1.2Mg alloys (Figures 1(a) through (d)) were prepared to separate and evaluate the influence of pores and hydrogen in the matrix on fracture behavior. The four Al-10.1Zn-1.2Mg alloys differ in their volume fraction of pores, V_F , and their hydrogen content, C_H . As shown in Figures 1(b) through (d), to vary the volume fraction of pores and the hydrogen content, thermal cycle (TC) processes were performed in air and in a vacuum. The temperature range of the thermal cycle was 653 K to 753 K, the heating rate was 0.028 K/s, and the number of cycles was set to 10. The TC process was carried out in air (during which the volume fraction of pores increased) or in a vacuum of 10^{-5} Pa (during which the hydrogen content and the volume fraction of pores decreased).

A thermal desorption apparatus equipped with a gas chromatograph (NISSHA FIS, Inc., PDHA-1000) was used to measure the hydrogen content in the prepared Al-10.1Zn-1.2Mg alloys. The temperature range of TDA was from room temperature to 853 K and the heating rate was 0.025 K/s. In TDA of Al-10.1Zn-1.2 Mg alloys, the entire hydrogen in the material was not desorbed in a single analysis. When TDA was performed ten consecutive times on the same specimen, all of the hydrogen was still not desorbed, and 0.1 mass-ppm of hydrogen remained in the specimen. This is because the molecular hydrogen that filled the pores (with the highest binding energy among the trap sites^[21,40]) is not easily desorbed during TDA. As it is time consuming to perform TDA ten times for all specimens, the hydrogen content was defined using the total amount of hydrogen desorbed in one analysis in this study.

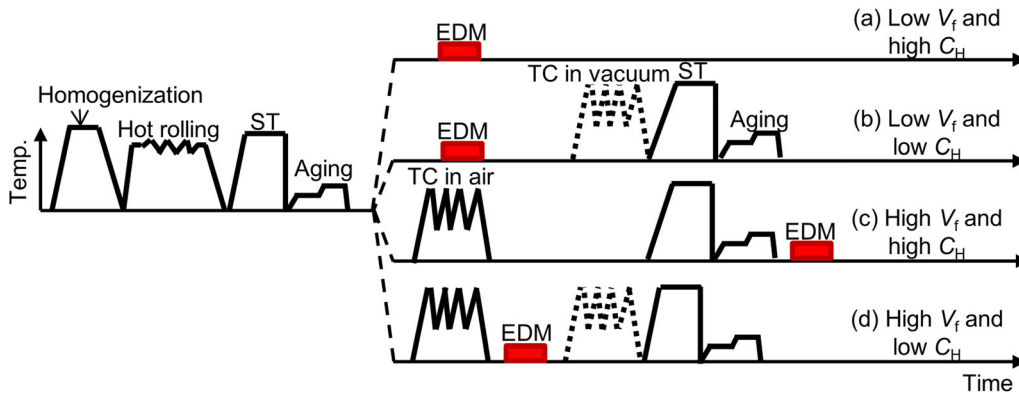


Fig. 1—Schematic of the process used to prepare four different Al-10.1Zn-1.2Mg alloys with different volume fractions of pores, V_f , and different hydrogen contents, C_H , as shown in (a) through (d). Thermal cycle (TC) in air was used to increase V_f , and TC in vacuum was used to decrease C_H .

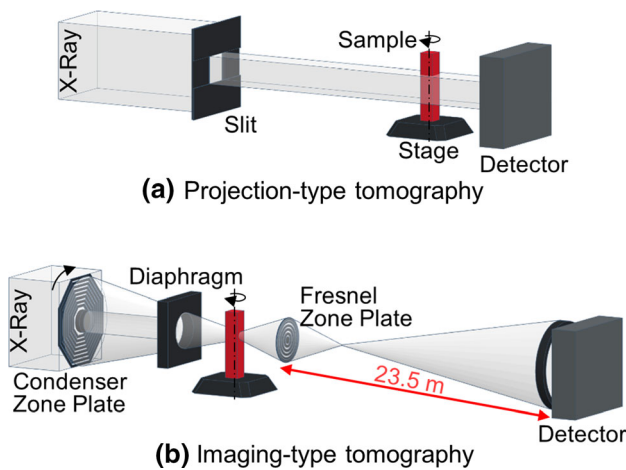


Fig. 2—Schematic of the (a) projection-type and (b) imaging-type tomography configurations performed on BL20XU and BL37XU of SPring-8, respectively.

B. Synchrotron X-Ray Imaging and In Situ Tests

In situ observations of fracture behavior via synchrotron X-ray tomography were performed on BL20XU and BL37XU of SPring-8, Japan. The projection-type tomography configuration shown in Figure 2(a) was employed to evaluate the fracture behavior of the entire material. To observe the intergranular and quasi-cleavage crack tips with higher resolution, the imaging-type tomography configuration shown in Figure 2(b) was used. The theoretical resolution was $1\ \mu\text{m}$ and $100\ \text{nm}$ for the projection-type and imaging-type tomography, respectively. The field of view of the projection-type tomography was $1024 \times 1024 \times 1024\ \mu\text{m}^3$, and the entire gauge-length region ($600 \times 600 \times 700\ \mu\text{m}^3$) of the specimen can be visualized completely in 3D. Although the resolution of imaging-type tomography is superior to that of projection-type tomography, its field of view is limited to a cylindrical region with a diameter of $83\ \mu\text{m}$ and a height of $59\ \mu\text{m}$. Therefore, imaging-type tomography was used to visualize the vicinity of the crack tips of the intergranular and quasi-cleavage cracks in 3D.

The X-ray was monochromated by a Si(111) double-crystal monochromator, and the energy was tuned to 20 keV. The detector consisted of a 2048×2048 pixel CMOS camera, an optical lens, and a scintillator. In the projection-type tomography, a $\text{Lu}_2\text{Al}_5\text{O}_{12}:\text{Ce}$ single crystal was used for the scintillator, and $\text{GdO}_2\text{S}:\text{Tb}$ was used in the imaging-type tomography. The distances between the specimen and the detector were 20 mm and 23.5 m in projection-type and imaging-type tomography, respectively. In addition, a condenser zone plate was used to locally improve X-ray flux, and an apodization Fresnel zone plate was used to focus the X-ray in the imaging-type tomography. These X-ray imaging elements were developed at SPring-8 for ultrahigh resolution X-ray imaging; the details are described elsewhere.^[41,42]

A small material testing machine (CT500, Deben UK Ltd.) was installed on the rotation stage of the X-ray tomography system, and the *in situ* observation of the fracture behavior was performed. In the tensile test, the initial strain rate was set at $3 \times 10^{-3}\ \text{s}^{-1}$ by displacement control, and the test was performed at room temperature. This strain rate corresponds to the lowest setting of the *in situ* testing machine used and was measured from the tomographic images of tensile test-piece before and after loading. It was necessary to temporarily stop the tensile loading and hold the displacement during tomography observation. Here, the holding time was 0.9 ks, and *in situ* tests were also performed in which the holding time was changed to 0.3 or 2.7 ks. In this experiment, *in situ* observations were carried out while holding the displacement for tensile strain increases of approximately 3 pct, which were repeated until fracture. The fracture surface was observed by a scanning electron microscope (SEM) after the tomographic experiments. A total of 1800 projection images were captured as the specimen was rotated by 180 degrees in steps of 0.1 degrees in tomographic observation, and these images were reconstructed into a 3D image by a convolution backprojection algorithm.

In addition, 2D projection images of growing cracks were continuously observed using both an *in situ* testing

machine and a projection-type tomography system. This *in situ* 2D imaging was performed to visualize the intergranular crack growth of an Al-10.1Zn-1.2 Mg alloy.

C. 3D Image analysis

Intergranular and quasi-cleavage cracks were extracted from 3D tomographic data and analyzed for morphology and crack tip opening displacement (CTOD). The CTOD was directly measured from 2D virtual cross sections of the extracted 3D crack image based on a report in the literature describing the measurement of the CTOD from a 3D tomographic image.^[43] In the 2D virtual cross sections of cracks, (i) the point of the crack tip was measured, (ii) lines were drawn upward and downward at 45 degrees from the crack tip until the lines contact the upper and lower surfaces of the crack, and (iii) the distance between the aforementioned contact points of the upper and lower crack surfaces was defined as the CTOD. The locations where the CTOD was measured depended on the morphology of the crack and were approximately 1 to 5 μm behind the crack tip. The details of the CTOD analysis of the crack inside the material are available elsewhere.^[43]

Furthermore, all the pores and particles in the specimens were analyzed in 3D, and their center of gravity, volume fraction, diameter, and surface area were calculated by the marching cubes algorithm that creates a 3D triangle model from a tomographic image.^[44] The molecular hydrogen content in the pores, C_{pore} , was estimated from the analyzed pore diameter^[12,14,17] and can be expressed by the energy balance of the surface energy and the internal pressure of hydrogen, $P = 4\gamma/d$, as follows:

$$C_{\text{pore}} = \sum \frac{2\pi\gamma d_i^2}{3RT}, \quad [3]$$

where d_i is the diameter of the i th pore, R is the gas constant, T is the temperature, and γ is the surface energy (1.16 J/m², which is the measured value for an Al(111) face^[14]). Recent FPSs revealed that the other surface energies are approximately 10 to 20 pct greater than that of the (111) surface.^[45] Because the (111) face of aluminum has the lowest surface energy, the estimation yields conservative lower limit values. Recent FPSs have clarified that the pore surface is a hydrogen adsorption trap site; however, this factor is not considered in Eq. [3],^[45] which applies only to the estimation of the molecular hydrogen inside the pores.

3D strain mapping inside the material was achieved using the physical displacements of the pores and particles, which were visualized by X-ray tomography.^[35] This calculation procedure of the strains is outlined below. First, identical pores and particles were tracked throughout loading using the matching parameter method.^[35] Next, tetrahedra with tracked particles as vertices were formed by Delaunay tessellation. Subsequently, various strain components were calculated from the deformation of a tetrahedron and

indicated its center of gravity. Further details of the matching parameter method and 3D strain mapping are available elsewhere.^[35]

III. RESULTS

A. Hydrogen Embrittlement Behavior

1. Microstructure and pores

Figure 3 shows the microstructure of the unloaded Al-10.1Zn-1.2Mg alloy as observed through projection-type tomography. The preparation process of the specimen shown in Figures 3(a) through (d) corresponds to subfigures (a) through (d) in Figures 1, respectively. Here, virtual cross sections of four representative specimens are shown, and each figure shows the volume fraction of pores, V_f , and the hydrogen content, C_H , as measured by TDA. Figure 3(a) shows a typical specimen without a thermal cycle. C_H is increased by EDM, and V_f is low. Second-phase particles on the micrometer scale were not observed. Relatively spherical pores were observed in Figures 3(c) and (d), on which thermal cycling was performed before solution treatment. The pores grew and C_H decreased during thermal cycling. The specimen shown in Figure 3(d) exhibited high V_f and low C_H because thermal cycling was applied after the EDM of the test piece. Thus, the combination of thermal cycling and EDM enabled us to prepare specimens with different V_f and C_H .

The mechanism by which the volume fraction of the pores changes during the TC process is considered as follows. As described in Section II-C, the internal pressure of the pore is estimated by $P = 4\gamma/d$. Assuming that the diameter of the pore is 3 μm and the surface energy is 1.16 J/m², the pressure is estimated as 1.5 MPa at room temperature. In the case of the TC process in air, it is believed that this internal pressure increases in a high-temperature environment to induce local creep deformation, causing the growth of pores.^[46] In contrast, in a TC process in vacuum, hydrogen is released from the specimen, and the pore pressure is also reduced according to Sieverts' law.^[40] In the TC process in vacuum, the internal pressure of the pores gradually decreases over time, and therefore the morphology of the pores is considered to have shrunk.

2. Changes due to the hydrogen content and the holding time

In this subsection, first, the changes in the HE behavior due to the hydrogen content are discussed based on the results of using specimens with a low V_f and high C_H and with low V_f and low C_H , as shown in Figures 3(a) and (b), respectively. Figure 4(a) shows the nominal stress–nominal strain curves in the tomographic *in situ* tensile test. It is found that the fracture strain was increased upon reducing the hydrogen content by the TC process. As shown in Figures 5(a) and (b), a reduction in the area fractions of intergranular and quasi-cleavage fracture were observed on the fracture surface due to the reduction of the hydrogen content. However, intergranular and quasi-cleavage

fractures still occurred in the alloy with reduced hydrogen content. The hydrogen content of this alloy was 0.41 mass ppm, and it was found that HE occurs at a hydrogen content that represents a practical level.^[47]

Next, the changes in the HE behavior due to the holding time are discussed based on the results of using the specimen with low V_f and high C_H , as shown in Figure 3(a). Figure 4(b) shows the nominal stress–nominal strain curves in the tomographic *in situ* tensile test. The three curves differ in the holding time of the tensile test. As described in the experimental section, it is necessary to hold the load and fix the displacement during the tomographic scan. The holding times were set to 0.3, 0.9, and 2.7 ks, as shown in Figure 4(b). The fracture strain was found to decrease with the increasing holding time. Cracks may grow during holding, which was observed in particular with a holding time of 2.7 ks. These fracture surfaces are shown in Figure 6. As shown in Figures 6(a) through (c), the area fractions of intergranular and quasi-cleavage fracture increased with the increasing holding time and decreasing fracture strain. At holding times of 0.3, 0.9, and 2.7 ks, the area fractions of quasi-cleavage fracture were 24, 19 and 38 pct, respectively, and the area fractions of intergranular fracture were 19, 58, and 61 pct, respectively.

The strain at which the cracks initiated was 15.8, 13.2 and 3.5 pct at holding times of 0.3, 0.9 and 2.7 ks, respectively. With the increasing holding time, the strain at which cracks initiated decreased. Cracks observed

through projection-type tomography are superimposed on the fracture surface, as shown in Figures 6(d) through (f). Three cracks captured at different strains are superimposed on each fracture surface in Figures 6(d) through (f). The crack that initially occurred, indicated by yellow, grows into the cracks indicated by green and blue depending on the loading. After the initial cracking, the increment of the applied displacement was 0.02 mm for three holding-time tests. Even though the applied displacement is the same, it was found that the crack grew rapidly as the holding time increased. All the initial cracks were intergranular cracks shown in the yellow crack in Figures 6(d) through (f), which transitioned to quasi-cleavage cracks and ductile cracks due to subsequent loading. The characteristic aspect of visualized crack growth is that the crack grew gradually in response to the given displacement rather than instantaneously advancing on one grain boundary or one facet.

The relation between the holding time and crack growth of the Al-9.9Zn-2.3Mg-1.4Cu alloy was previously investigated.^[9,12,36] The embrittlement became prominent as the holding time increased, similar to the behavior observed for the present Al-10.1Zn-1.2Mg alloy. However, in the cracks that formed the fracture surface, the initial crack was a quasi-cleavage crack. The influence of the holding time on the HE behavior is related to the local accumulation of hydrogen around the crack tips.

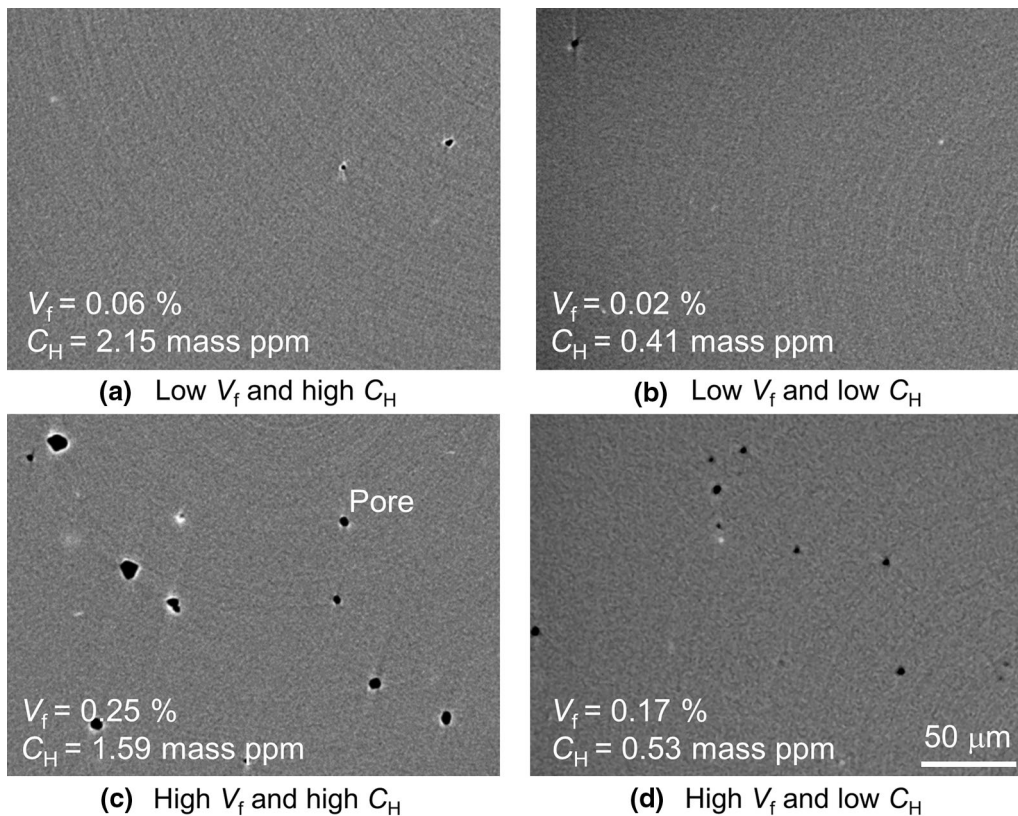
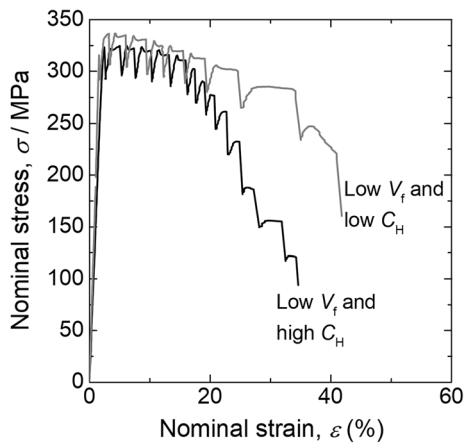
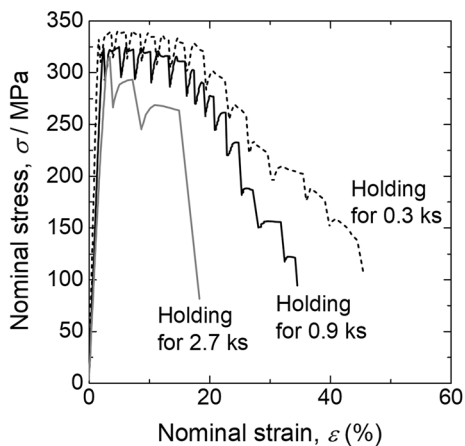


Fig. 3—Virtual cross sections of a 3D tomographic image at different volume fractions of pores, V_f , and hydrogen contents, C_H , in Al-10.1Zn-1.2Mg alloys. Each image was captured in the unloaded state. The preparation processes in (a) through (d) correspond to Figs. 1(a) through (d), respectively.



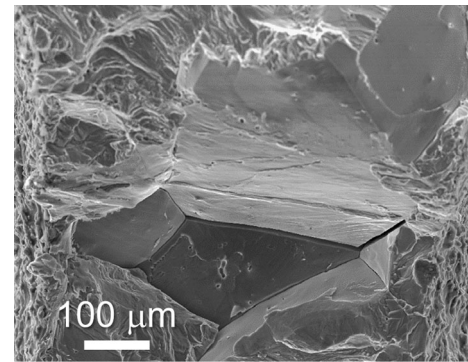
(a)



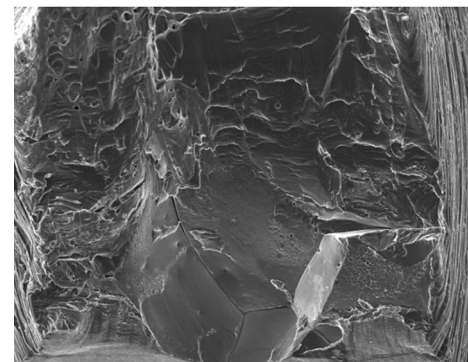
(b)

Fig. 4—Nominal stress–strain curves obtained by *in situ* tensile tests. The curves in (a) were obtained from a low V_f and high C_H alloy and a low V_f and low C_H alloy shown in Figs. 3(a) and (b), respectively, at the holding time of 0.9 ks. (b) was obtained from low V_f and high C_H alloys shown in Figs. 3(a) at the different holding times of 0.3, 0.9, and 2.7 ks.

To investigate the relationship between the hydrogen accumulation and intergranular fracture more deeply, a high-hydrogen Al-10.1Zn-1.2 Mg alloy was subjected to EDM twice on the surface. The hydrogen content of this specimen, as measured by TDA, was 25.4 mass ppm. No blisters formed on the surface, even with twice the hydrogen charging, and hydrogen was considered to be present in matrix trap sites such as the grain boundaries, vacancies, and dislocations. This specimen with a high hydrogen content was mounted onto an *in situ* tensile test machine, and the intergranular crack growth under constant displacement was 2D-imaged. A monotonic tensile load was applied to the specimen until cracking occurred. The applied strain measured from the projection images was 4.5 pct. Then, the loading was stopped, and X-ray projection images continued to be captured under constant displacement. The X-ray projection images of the specimen before and after cracking are shown in Figure 7. The times shown in Figures 7(b) through (d) are the time elapsed after the displacement was fixed. As is evident in Figures 7(a) and (b), the



(a) Low V_f and high C_H



(b) Low V_f and low C_H

Fig. 5—Fracture surfaces of the (a) low V_f and high C_H alloy and (b) low V_f and low C_H alloy shown in Figs. 3(a) and (b) after *in situ* tensile tests, respectively, with a holding time of 0.9 ks.

monotonic tensile load introduced multiple cracks into the specimen. Figures 7(c) and (d) show 2D projection images after 65 and 130 seconds elapsed from Figure 7(b) with the displacement fixed. As indicated by the red arrows, continuous intergranular crack progression was observed even when the displacement was fixed. The growth rate was approximately $1 \mu\text{m/s}$, and the crack tip was sharp. The influence of the holding time and the hydrogen content on the HE behavior is related to the local accumulation of hydrogen around the crack tips, which is discussed in detail later.

3. Effect of particles

Figures 8(a) and (b) show tomographic virtual cross sections of the Al-10.1Zn-1.2Mg alloy without and with trace iron, respectively. Figures 8(c) and (d) show their fracture surfaces after the tensile test at a holding time of 0.9 ks. The emission spectrochemical analysis of this specimen was performed, but the increased Fe content was outside the detection range of the device (*i.e.*, below 0.01 mass pct). The existence of the particles shown with white contrast in Figure 8(b) is confirmed. As a result of the SEM-EDX analysis, the average chemical composition of the particles was determined to be $\text{Al}_{79}\text{Fe}_{14}\text{Zn}_7$. Homogenization and solution treatment of Al-10.1 Zn-1.2Mg were performed at 773 K. On the basis of the isothermal section at 773 K of the Al-Zn-Fe ternary phase diagram,^[48] this particle is presumed to be Zn-bearing $\text{Fe}_4\text{Al}_{13}$. The volume fractions of pores

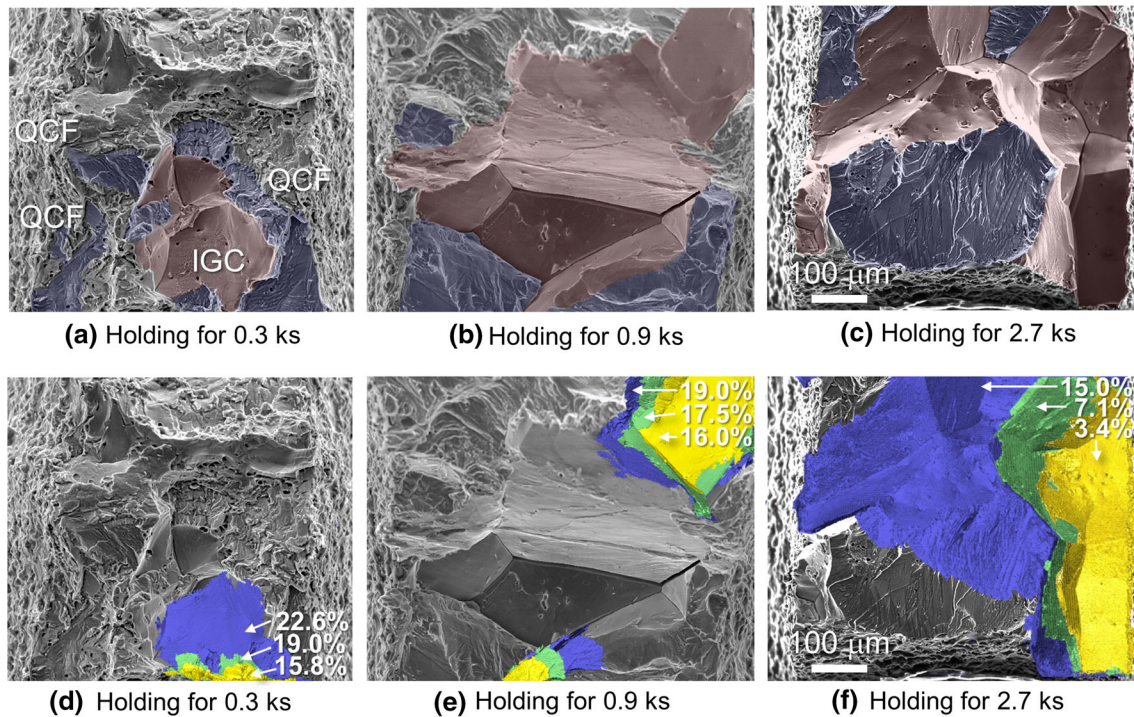


Fig. 6—Fracture surface of tensile specimens at different holding times. In (a) through (c), intergranular and quasi-cleavage fractured regions are indicated in red and blue, respectively. In (d) through (f), cracks visualized by projection-type tomography at each strain are superimposed as yellow, green, and blue. Nominal strains are also indicated when each crack was visualized by projection-type tomography (Color figure online).

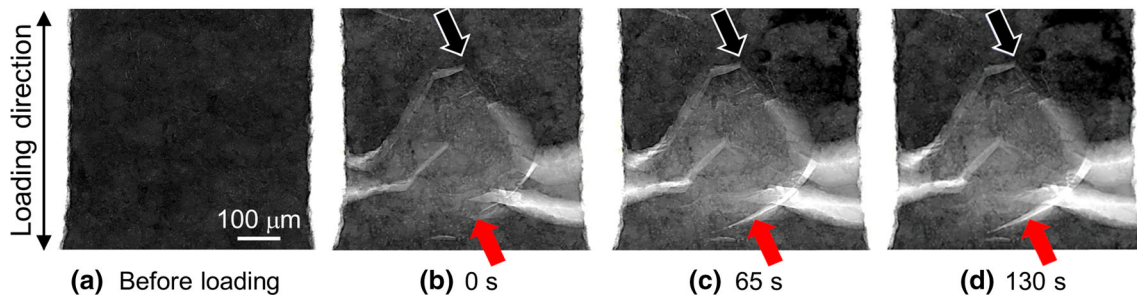


Fig. 7—2D projection images of specimen (a) before loading at (b) 0, (c) 65, and (d) 130 s after holding the displacement. The crack indicated by the black arrow was arrested, and the crack indicated by the red arrow grew even though the displacement was constant (Color figure online).

and particles and the hydrogen content were 0.08, 0.41 pct, and 2.08 mass ppm, respectively. The number density of particles was also analyzed three-dimensionally from the tomographic volume and was found to be $8.35 \times 10^{13} \text{ m}^{-3}$. If the particles are assumed to be uniformly dispersed inside a specimen, the average nearest-neighbor distance of the particles is 28 μm .

The fracture surface shown in Figure 8(d) is remarkably different from that in Figure 8(c), although the volume fraction of pores and the hydrogen content are equivalent to those of the alloy without trace iron. Relative to Figure 8(c), the intergranular and quasi-cleavage fractured areas in Figure 8(d) were reduced, and a dimple fracture was observed. TDA was conducted to evaluate the change of the fracture surfaces with and without particles from the viewpoint of hydrogen trapping on particles. The hydrogen desorption curves of these specimens are shown in Figure 9.

Identification of the TDA peaks of aluminum alloys is not simple. For example, interpretations differ among researchers as to whether the maximum peak at approximately 830 K is the peak of hydrogen desorbed from pores or that of hydrogen desorbed from vacancies.^[19,49,50] The heat of dissolution of molecular hydrogen, the binding energy of adsorbed hydrogen on aluminum surface, and the binding energy of vacancies have been calculated by recent first-principles calculations as 0.68, 0.60 eV at maximum, and 0.30 eV, respectively.^[21] Given the aforementioned order, this maximum peak likely corresponds to the hydrogen desorbed from the pores. Pores often heterogeneously nucleate on micron-scale particles in aluminum alloys during heat treatment.^[14,17,51] The volume fraction of pores increased from 0.06 to 0.08 pct because the micron-scale particles (*i.e.*, the nucleation sites of pores) increased in the Al-Zn-Mg alloy with trace iron, leading

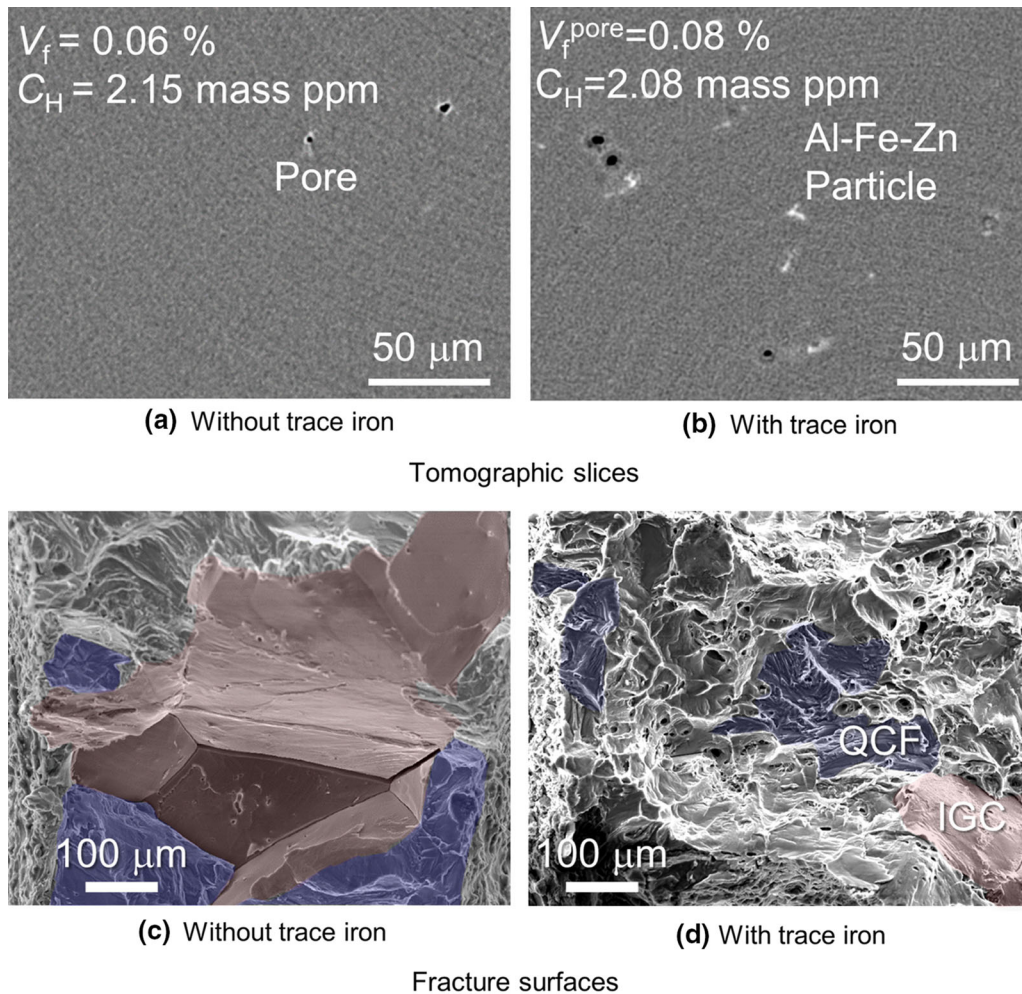


Fig. 8—Tomographic slices and fracture surfaces of Al-10.1Zn-1.2Mg alloys (*a* and *c*) without and (*b* and *d*) with trace iron, respectively. The fracture surface without trace iron corresponds to Fig. 6(b). The intergranular and quasi-cleavage fractured regions are shown in red and blue, respectively (Color figure online).

to the peak at approximately 830 K in Figure 9(a). Furthermore, as evident in Figure 9(b), a broad peak was observed in the temperature range from 650 K to 730 K in the Al-Zn-Mg alloy. In this temperature range, vacancy concentration, dislocation density, and grain size change. We considered that both the changes in the trap-site densities and the hydrogen desorption from the trap sites occurred, resulting in several overlapping desorption peaks observed as a broad peak. On the other hand, the peak at 714 K observed for the Al-Zn-Mg alloy with trace iron is sharp compared with the broad peak for the Al-Zn-Mg alloy without iron. Particles in the Al-Zn-Mg alloy with trace iron were formed during solidification and were not dissolved in the matrix during homogenization and solution treatment at 773 K for 7.2 ks. Therefore, in the temperature range of 650 K to 730 K, the structural variation of particles is considered to be minor relative to the variations of vacancies, dislocations and grain sizes. Given the aforementioned viewpoints, diffusible hydrogen trapped at grain boundaries, dislocations or vacancies partitioning to particles would explain the changes

in the hydrogen desorption curves in Figure 9(b) due to particles.

The results from Figures 8 and 9 indicate that intergranular and quasi-cleavage fractures can be suppressed by preferentially trapping hydrogen in the particles even though the hydrogen content in the whole material is constant. Regarding suppression of intergranular and quasi-cleavage fractures by particles, the same tendency as the present result also appeared in an Al-9.9Zn-2.3Mg-1.4Cu alloy. Su *et al.* investigated the influence of particles on HE behavior by preparing Al-9.9Zn-2.3Mg-1.4Cu alloys with different Fe and Si contents.^[36] Based on their tensile tests, the area fractions of quasi-cleavage fracture were 38, 30 and 28 pct in the specimens having both Fe and Si contents of 0.01, 0.05 and 0.3 mass pct, respectively. In specimens where the contents of Fe and Si are high and Al₇Cu₂Fe and Mg₂Si particles are distributed at high density, intergranular and quasi-cleavage fractures are suppressed. For this reason, Su *et al.* considered that the amount of hydrogen trapped at dislocations and at the crack tip decreases in a relative sense depending on the

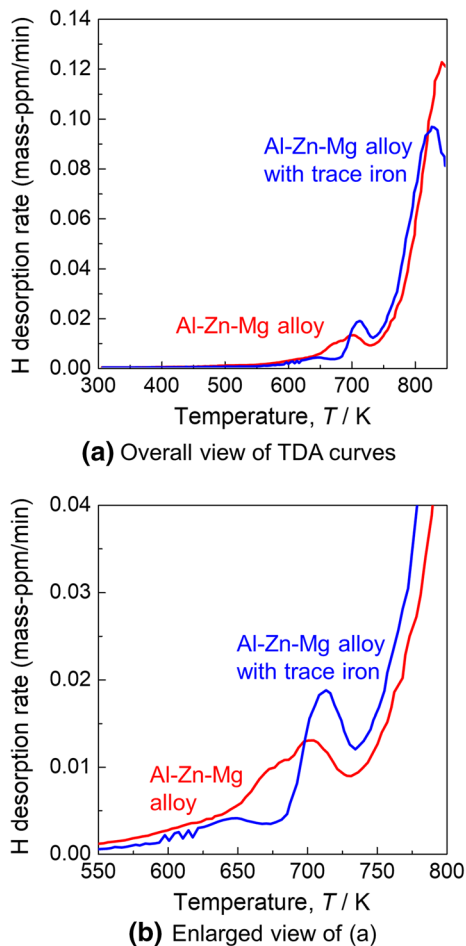


Fig. 9—Thermal desorption curves of the Al-Zn-Mg alloy and Al-Zn-Mg alloy with trace iron. (a) An overall view of thermal desorption curves. (b) An enlarged view of (a) in the temperature range from 550 K to 800 K (Color figure online).

particles. Therefore, the quasi-cleavage fracture could be suppressed, which is consistent with the present experimental results using Al-10.1Zn-1.2Mg alloys.

The hydrogen trap sites of $\text{Al}_7\text{Cu}_2\text{Fe}$ and Mg_2Si are still unclear. Hydrogen trap sites related to particles include sites inside the particles, at coherent/semicoherent/incoherent interfaces, and within strain fields around the particles,^[52–56] but the ones that apply to $\text{Al}_7\text{Cu}_2\text{Fe}$ and Mg_2Si are not yet understood. Currently, we are promoting research focusing on the possibility of hydrogen trapping inside particles, and the results will be published in the future.

4. Influences of atomic hydrogen and pores

As mentioned in the introduction, pores in aluminum have been reported to affect the mechanical properties.^[17] This report revealed the role of pores in ductile fracture, but the role of the pores in HE is still unclear. The inside of the pore is filled with molecular hydrogen,

and its hydrogen content is expressed by Eq. [3]. Therefore, the pores in aluminum alloys can be regarded as containing molecular hydrogen. In this subsection, the effects of atomic hydrogen and molecular hydrogen are separately evaluated from the viewpoint of the HE behavior.

Tomographic *in situ* tensile tests were performed by means of several specimens with different volume fractions of pores and hydrogen content in the matrix, as shown in Figure 3. The four specimens shown in Figure 3 are representative, and eight other specimens (Two specimens for each step in the process of (a) to (d) in Figure 1) were also prepared. Tomographic *in situ* tests were not performed on these eight specimens, but the tomographic observation of the pores was performed to estimate the molecular hydrogen content at no loading. Following this, the hydrogen embrittlement behavior was investigated in the laboratory under the same tensile conditions as those of the tomographic *in situ* tests. Here, the holding time was set to be 0.3 ks. After this holding time, the fracture surfaces were observed by SEM, and the area fractions of the intergranular and quasi-cleavage fracture surfaces were analyzed. The hydrogen content in each specimen was also analyzed by TDA, and the area fractions of intergranular and quasi-cleavage fractures, total hydrogen content, and molecular hydrogen content in a total of 12 specimens were investigated. To evaluate the effects of atomic hydrogen and molecular hydrogen on the HE, the hydrogen content in the matrix, C_{mat} , was defined as follows:

$$C_{\text{mat}} = C_{\text{total}} - C_{\text{pores}}, \quad [4]$$

where C_{total} is the total hydrogen content of each specimen as measured by TDA.

The area fractions of ductile, quasi-cleavage, and intergranular fractures are summarized in terms of the hydrogen content in the matrix and the pores, and the results are described in Figure 10. Here, a contour map shows the area fractions of each fracture mode. Ductile fracture in Figure 10 was defined as a fracture surface that is neither intergranular fracture nor quasi-cleavage fracture. As the hydrogen content in the matrix increases, the ductile fracture transitions to a quasi-cleavage fracture. When the content increases further, intergranular fracture tends to occur. In contrast, it has been clarified that the role of the hydrogen content in pores is minor in the transition of fracture modes. With regard to the ductile fracture of an AA2024 alloy at room temperature and an AA5086 alloy at high temperature, it has been reported that the growth and coalescence of pores dominate the fracture behavior.^[17,51] Even with the same aluminum-based alloys, the high-hydrogen Al-10.1Zn-1.2Mg alloy undergoes HE, resulting in intergranular and/or quasi-cleavage fractures. It can be concluded that the influence of pores on fracture is small since HE occurs before the growth and coalescence of pores.

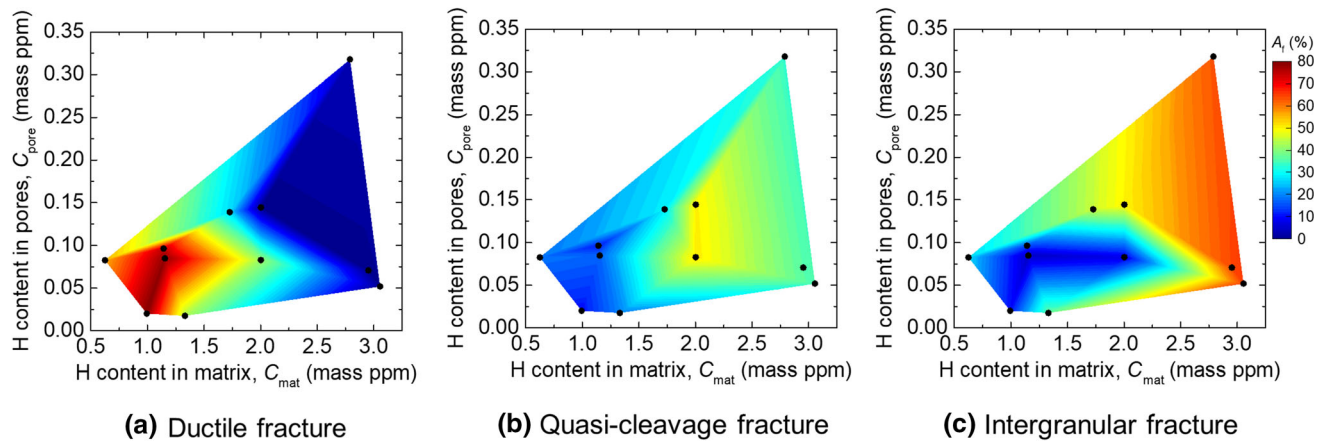


Fig. 10—Contour map of the area fraction, A_f , of (a) ductile, (b) quasi-cleavage, and (c) intergranular fractured regions on the fracture surface. The hydrogen content in the pores was analyzed by 3D tomographic images; the hydrogen content in the matrix, C_{mat} , is equal to the total hydrogen content minus the hydrogen content in the pores (Color figure online).

B. Local Deformation and Fracture Behavior Around Cracks

1. 3D strain mapping ahead of the crack tip

As described in Section III-A, it was found that the Al-10.1Zn-1.2Mg alloy exhibits HE, which is dominated by the hydrogen content in the matrix. However, the fracture behavior is not completely brittle. The SS curves in Figure 4 and the crack growth behavior in Figure 6 imply that intergranular and quasi-cleavage crack growths of Al-10.1Zn-1.2Mg alloy accompany plastic deformation. Because the region where the fracture occurs is a crack tip, it is important to quantitatively evaluate the local plastic deformation near crack tips.

In this study, various strain components around the crack tips were analyzed using a 3D strain mapping technique.^[35] *In situ* holding-time tests of Al-10.1Zn-1.2Mg alloy and Al-9.9Zn-2.3Mg-1.4Cu alloy were performed to initiate intergranular cracks and quasi-cleavage cracks, respectively. After the cracks were initiated, 3 pct strain was applied to analyze the strain distribution ahead of the crack tips. The lengths of the visualized cracks were approximately 70 and 50 μm for the intergranular and quasi-cleavage cracks, respectively. Figures 11(a) and (b) show the 3D scatter plots of hydrostatic strain, equivalent strain, and normalized-equivalent strain ahead of crack tips when 3 pct strain was applied after cracking. Here, normalized-equivalent strain means the equivalent strain, which is divided by the average equivalent strain of the whole material to investigate the strain localization. As described in the methodology, each strain component inside materials was calculated on the basis of the physical displacements of pores and particles. Hydrostatic strain, equivalent strain, and normalized-equivalent strain were plotted at the position corresponding to the center of gravity of the tetrahedron with pores and particles as vertices in Figure 11. The color of the markers in each plot corresponds to the value of each

strain component displayed in the color bar. The coordinates in Figures 11(a) and (b) are the absolute coordinates of the 3D region captured by projection-type tomography, and the right side of the figures is located at the specimen surface.

In the intergranular crack shown in Figure 11(a), localization of each strain component could not be analyzed in the vicinity of the crack tip or the regions distant from the crack. There were regions where equivalent and normalized-equivalent strains were high, as shown in the quasi-cleavage crack shown in Figure 11(b). Note that this localization of strain does not depend on the presence of a crack. As in the previous findings for the Al-9.9Zn-2.3Mg-1.4Cu alloy,^[12] a strain-localized region was first formed, and a crack grew along the localized region. Thus, localization of the strain caused by the crack appeared in neither intergranular nor quasi-cleavage cracks.

2. 3D crack morphology

Morphologies of intergranular and quasi-cleavage cracks were visualized in detail by imaging-type tomography. *In situ* holding-time tests were performed until the intergranular and the quasi-cleavage crack initiations occurred in Al-10.1Zn-1.2Mg alloy and Al-9.9Zn-2.3Mg-1.4Cu alloy, respectively, and then, their crack tips were visualized in 3D. The spatial resolution of imaging-type tomography is improved fivefold compared with projection-type tomography; however, the field of view is limited. Because the entire specimen could not be visualized, the applied strain could not be measured from the tomographic image; however, displacements were applied until the crack initiations in Al-10.1Zn-1.2Mg alloy and Al-9.9Zn-2.3Mg-1.4Cu alloy were 0.08 and 0.19 mm, respectively. The vicinities of the tips of an intergranular crack and a quasi-cleavage crack are shown in Figures 12 and 13, respectively. In the imaging-type tomography, the field of view is a cylindrical region (*i.e.*, 83 μm in diameter,

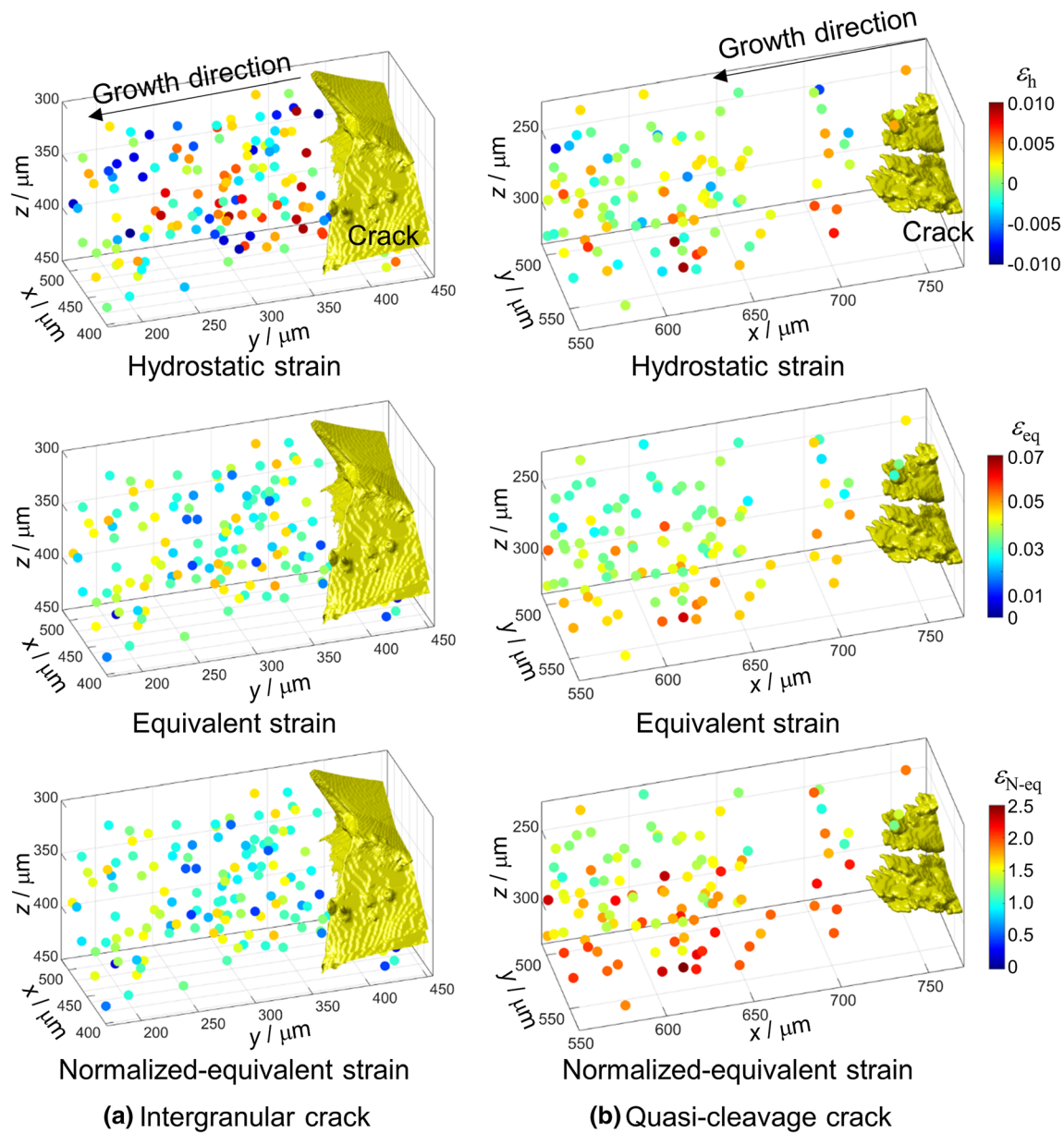


Fig. 11—3D strain mapping of hydrostatic, equivalent, and normalized-equivalent strains. Each strain component around a crack tip corresponding to (a) intergranular and (b) quasi-cleavage cracks is represented. The position of each marker is the position of the center of gravity of a tetrahedron composed of pores and particles; the color corresponds to the value of each strain component indicated by the color map (Color figure online).

59 μm in length) near the crack tip because the region of interest inside the specimen was imaged. Therefore, the semicircular contours in Figures 12(a) and 13(a) are the edges of the field of view, and the crack tip is the zigzag edge located in the upper region.

The 3D image and the 2D virtual cross section shown in Figures 12(a), (b), (c) and (e), respectively, show that the tip of the intergranular crack is sharp and flat compared with the quasi-cleavage crack shown in Figure 13. Crack deflection was observed near the crack tip in Figures 12(d) and (e); conceivably, however, the crack may have grown through the neighboring grain. The deflection point corresponds to the triple junction point of the grain boundary. The quasi-cleavage crack

shown in Figure 13 exhibits a tortuous morphology relative to the intergranular crack. The appearance of the crack propagating while repeatedly blunting locally and sharpening was visualized. The crack tips and the intergranular cracks are sharp, whereas the quasi-cleavage crack exhibits a rugged surface. Figure 14(a) shows the fracture surface of Al-9.9Zn-2.3Mg-1.4Cu alloy observed by SEM, and Figure 14(b) shows an image obtained by superimposing the crack of Figure 13 and the enlarged fracture surface of Figure 14(a). The rugged surface morphology of the quasi-cleavage crack shown in Figure 13 coincides with the quasi-cleavage facet. With regard to the mechanism of the quasi-cleavage facet formation of steel, the nucleation and growth

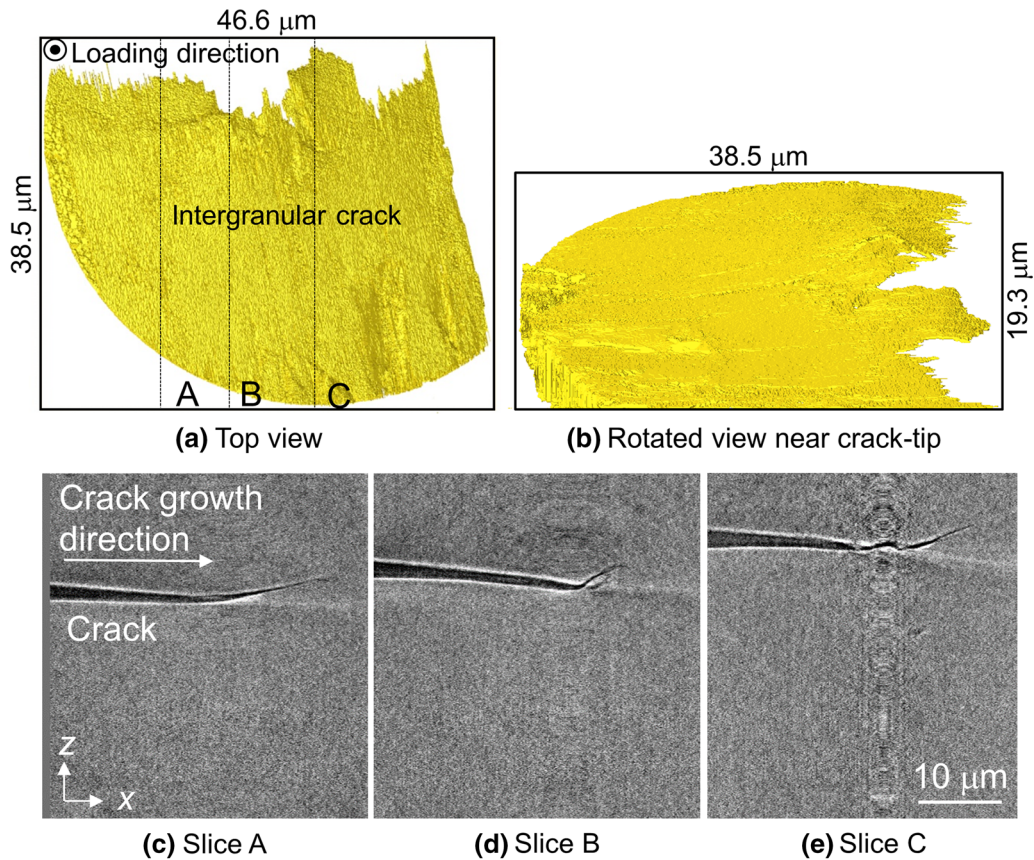


Fig. 12—3D tomographic images of an intergranular crack ((a) top and (b) side views). In (c) through (e), the 2D virtual cross sections of A, B, and C correspond to the dashed line in the top view (Color figure online).

of nanovoids at the intersection of the slip band ahead of the crack tip have been proposed.^[33] However, as shown in Figure 13, no void exceeding 300 nm is observed ahead of the quasi-cleavage crack tip for the Al-9.9Zn-2.3Mg-1.4Cu alloy. Approximately 5-30-nm nanovoids were observed in the strain-localized region in the TEM and the HAADF-STEM images of Al-9.9Zn-2.3Mg-1.4Cu alloy after 5 pct strain, as previously reported.^[12] In addition, the growth behavior of nanovoids of Al-9.9Zn-2.3Mg-1.4Cu alloy has been analyzed using imaging-type tomography.^[57] The nanovoids are uniformly distributed in the strain-localized region, and the accumulation and coalescence of nanovoids was not observed during deformation. We inferred that nanovoids mainly act as one of the main hydrogen trap sites in and play a significant role in the repartitioning behavior of hydrogen in the Al-9.9Zn-2.3Mg-1.4Cu alloy. We are currently investigating the origin of quasi-cleavage facets. One of the candidates is the interfacial decohesion of Al/MgZn₂ due to hydrogen accumulation at the Al/MgZn₂ interface. Tsuru *et al.* determined by FPS that the interfacial decohesion of MgZn₂ precipitates initiate when the trapped hydrogen at the Al/MgZn₂ interface reaches 18.9 atom H/nm².^[58] The experimental verification of

the above calculation is ongoing and will be published in the future.

The CTOD was directly measured from the 2D virtual cross section of the 3D crack visualized by imaging-type tomography.^[43] Figures 15(a) and (b) show the distributions of the CTOD for mode I (hereinafter CTOD_I) along the crack front lines of Figures 12(a) and 13(a), respectively. The average CTOD_I values of the intergranular and quasi-cleavage cracks were 0.14 and 0.23 μm, respectively. In the quasi-cleavage crack, CTOD_I was locally as high as approximately 1 μm in a blunted region, as shown in Figure 13(d). The results presented here imply that the HE crack growth of aluminum alloys occurs with small crack driving forces.

IV. DISCUSSION

A. Hydrogen accumulation and fracture behavior

The mechanism behind the increase in holding time and HE behavior, as observed in Figures 4 and 6, is considered to be hydrogen accumulation and hydrogen repartitioning in the plastic zone. As mentioned in the introduction, hydrogen localizes to slip lines and grain boundaries by plastic deformation and accumulates over

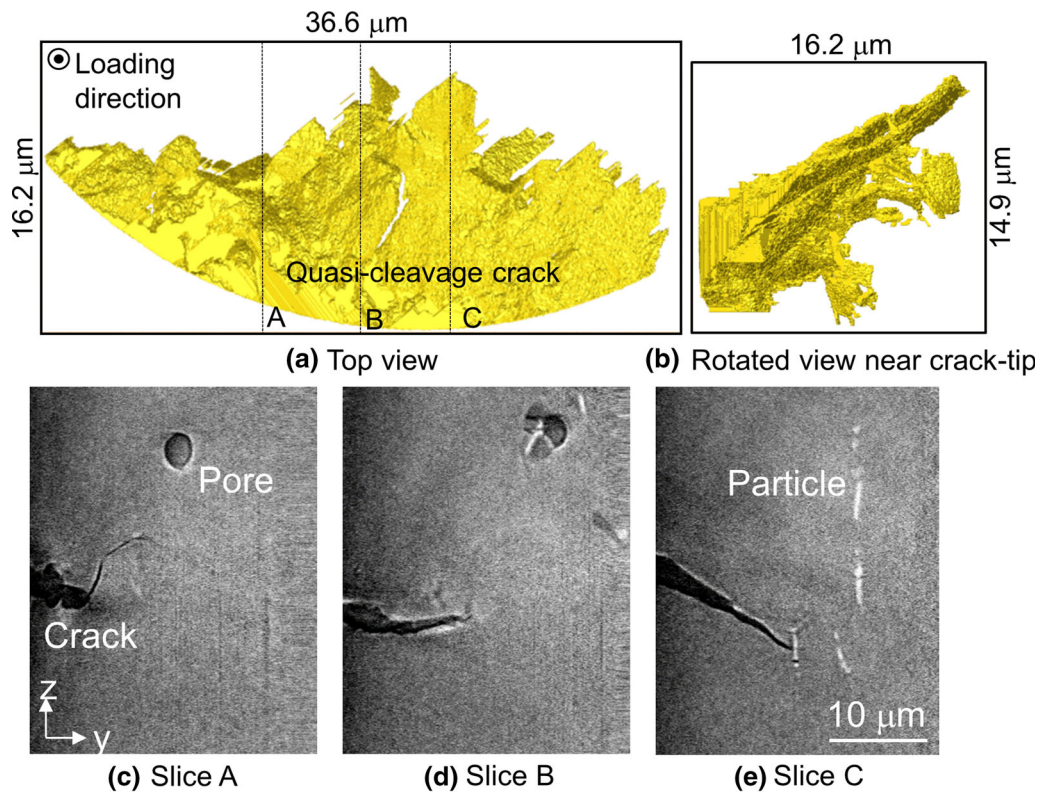
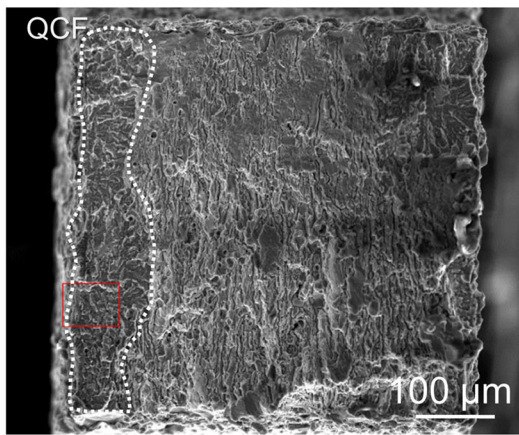


Fig. 13—3D tomographic images of a quasi-cleavage crack ((a) top and (b) side views). In (c) through (e), the 2D virtual cross sections of A, B, and C correspond to the dashed line in the top view (Color figure online).

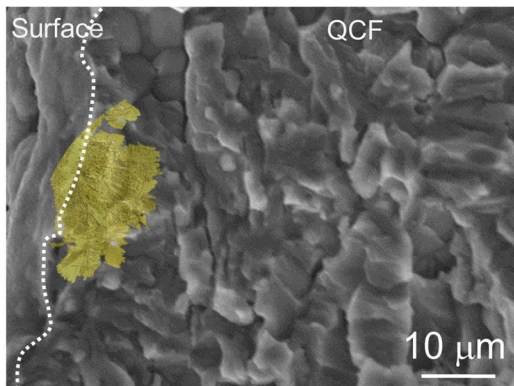
time at room temperature.^[22–26] Understandably, the diffusion of hydrogen in aluminum is necessary for its accumulation at specific sites. Numerous reports on the diffusion coefficient of hydrogen in aluminum have appeared in the literature.^[37,38,50] The coefficient derived by Eichenauer and Pebler is considered the most appropriate and is expressed as $D = 2.1 \times 10^{-5} \exp(-Q/RT)$,^[37,38] where D (m^2/s) is the diffusion coefficient of the hydrogen in aluminum and Q is the activation energy of diffusion, equal to 45.63 kJ/mol. The diffusivity at 298 K is $2.1 \times 10^{-13} \text{ m}^2/\text{s}$ from this simple estimation; however, the effect of trapping on the hydrogen diffusion is ignored. Al-Zn-Mg alloys have various hydrogen trap sites such as vacancies and grain boundaries. As mentioned in Section 2.1, the effective diffusivity of overaged Al-6.9 pct Zn-2.65 pct Mg-0.06 pct Cu alloy has been reported to be $1.05 \times 10^{-11} \text{ m}^2/\text{s}$ at 298 K.^[39] In view of this, we speculate that the aforementioned diffusivity of $2.1 \times 10^{-13} \text{ m}^2/\text{s}$ is conservative. The diffusion distance, l , in 2.7 ks, which is the holding time for the tomography *in situ* tensile loading, is estimated to be $(2Dt)^{1/2}$, which is $34 \mu\text{m}$ at 298 K. Hydrogen is reasonably inferred to accumulate at the crack tip by diffusion with a holding time of 2.7 ks, even at room temperature. Notably, when cracks initiate during holding-time tests, stress-induced diffusion occurs because a hydrostatic stress field appears at the crack tip.^[59] Conceivably, hydrogen is transported to the vicinity of the crack tip from the region more than $34 \mu\text{m}$ away during holding, but this scenario is not

considered. Again, the estimation of the diffusion in the present work is conservative.

We show the crack growth behavior under a fixed displacement in the specimen with a high hydrogen content in Figure 7. We will discuss the influence of hydrogen on this crack growth behavior. First, to measure the 3D morphology by X-ray tomography, it is necessary to hold the specimen stationary during a tomographic scan. Spontaneously propagating cracks, as in Figure 7, cannot be observed by tomography, and that is why the 2D observation of projection images was performed. Ideally, this crack propagation behavior should be analyzed quantitatively using fracture mechanics parameters. However, there are multiple intergranular cracks shown in Figure 7, and they are deflected. The 3D morphology is also unclear, and quantitative evaluation is difficult. Therefore, the crack growth behavior is qualitatively discussed below by considering the local stress intensity factor of the crack tip, k . The stress intensity factor, K , which is one of the fracture mechanics parameters that indicates the crack driving force, is expressed as $K = F\sigma\sqrt{\pi a}$ using the geometrical factor, F , the stress, σ , and the crack length, a . The mathematical definition of k is the same as K , but lowercase k is used as a local parameter in this discussion. The local crack driving force, k , slightly increases if the crack grows $100 \mu\text{m}$ under constant stress. However, because the displacement was fixed in the experiment of Figure 7, the stress dropped markedly due to crack growth, as shown in Figure 4. Therefore, k



(a) Overall view



(b) Enlarged view of rectangular region in (a)

Fig. 14—Fracture surface of Al-9.9Zn-2.3Mg-1.4Cu alloy observed by SEM. (a) The overall view of fracture surface and (b) the enlarged view of rectangular region in (a). In (b), the quasi-cleavage crack captured by imaging-type tomography is superimposed (Color figure online).

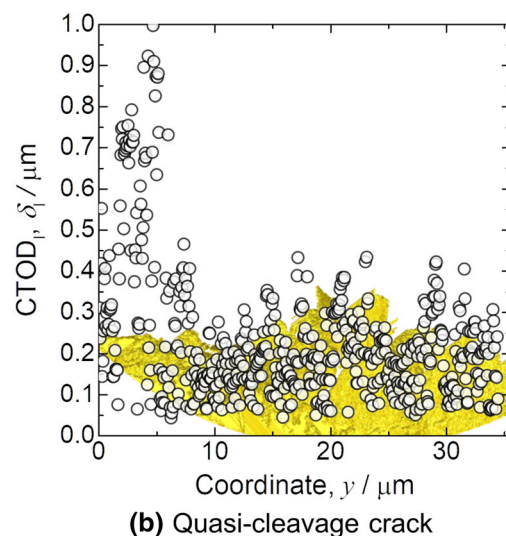
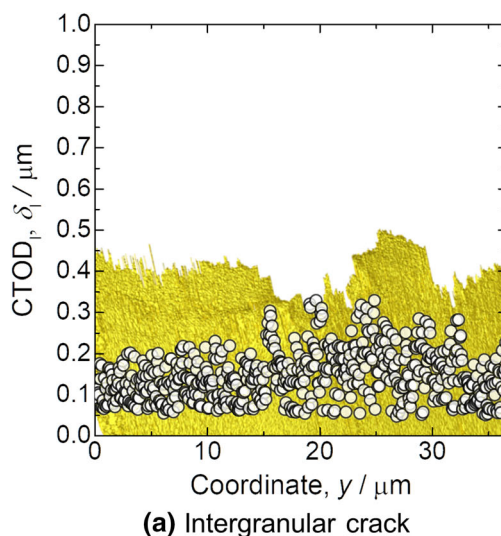


Fig. 15—Variations in local crack driving forces, $CTOD_I$, along the (a) intergranular and (b) quasi-cleavage crack front lines. $CTOD_I$ is directly analyzed from the crack tip morphology (Color figure online).

at the crack tip shown in Figure 7 decreased over time, but the crack did not arrest. The crack growth behavior indicated by the red arrow cannot be interpreted by the fracture mechanics parameters alone, suggesting that the accumulation of hydrogen reduced the local crack growth resistance at the grain boundary and that crack growth under constant displacement occurred. On the other hand, the intergranular crack indicated by black arrows did not grow. The difference in the behaviors of intergranular crack growth can be attributed to the influence of the grain boundary character. Hirayama *et al.* investigated the relation between the intergranular cracking and the crystallographic properties of an Al-10.1-Zn-1.2Mg alloy of the same composition as used in the present study.^[60] According to their study, intergranular cracks tended to initiate at the grain boundary, where both the relative misorientation and geometric angle to the tensile axis are large. That is, fracture easily occurs at the grain boundary where the local stress of mode I acts and traps hydrogen due to the high relative misorientation. Further crystallographic analysis is ongoing and will be published elsewhere.^[60]

An FPS that concluded that hydrogen segregation occurs at the grain boundary with a relatively high grain-boundary energy was reported for iron and aluminum.^[29] Furthermore, a recent FPS revealed that as the trapped hydrogen in the grain boundary reaches 22 H atoms/nm², the grain-boundary cohesive energy decreases from 1.4 to 0.2 J/m², causing intergranular fracture in the aluminum.^[45] In the results shown in Figure 7, it is conceivable that the grain boundaries indicated by the red arrows tend to trap hydrogen and locally exhibit high hydrogen contents at the intergranular crack tips. Therefore, crack growth occurred even under fixed displacement. G. Bond *et al.* investigated crack growth under fixed displacements by means of

TEM specimens of A7075 alloy and pure aluminum (99.999 pct) in a hydrogen environment. It was reported that crack growth occurred immediately when 3–11 kPa of hydrogen gas was introduced into the TEM sample chamber. The results in Figure 7 and those of G. Bond *et al.* seem to be analogous, but the crack growth conditions are completely different in terms of the specimen size and hydrogen trap state. For the crack growth in Figure 7, hydrogen trapped inside the material was the driving force, and growth was not governed by the gas environment outside the specimen. Furthermore, the crack growth was observed by means of the foil specimens, and not in the bulk. Crack growth behavior tends to be influenced by the geometry, the various internal stress and strain states, and the surface conditions of the test piece. Therefore, the behavior of the crack growth observed in the foil is not necessarily the same as that in the bulk. Figure 7 is the experimental visualization of crack growth under fixed displacement by hydrogen accumulation using a bulk specimen.

B. Local Deformation at the Intergranular and Quasi-cleavage Crack Tip

No strain components concentrated at the vicinity of the crack tip were observed in either the intergranular crack or the quasi-cleavage crack in the strain map shown in Figure 11. This strain map is based on the microstructural feature tracking technique, where the changes in the displacement of pores and particles around the crack are tracked.^[35] The nearest-neighbor distance of each pore and particle is approximately 18 μm in the materials used in this study. Therefore, the strain mapping shown in Figure 11 cannot analyze a strain field smaller than 18 μm . The CTODs measured by imaging-type tomography were as small as 1 μm at the maximum, as shown in Figure 15. The process zone of the crack tip is reasonably inferred to be smaller than 2 μm when the size of process zone is estimated as twice the CTOD. Thus, due to the sharp crack tip without blunting and the small process zone, the plastic region caused by the crack may be smaller than 18 μm . Consequently, strain mapping based on microstructural feature tracking apparently could not assess the local displacement field at the crack tip.

The stress and strain field at the crack tip follows the Hutchinson-Rice-Rosengren (HRR) singularity in the stationary crack and Rice-Drugan-Sham (RDS) singularity in the growing crack.^[61–63] The HRR solution is derived by elastoplastic analysis of the crack tip region based on total strain theory and is expressed as follows:

$$\delta = 2\alpha' \varepsilon_0 \left(\frac{J}{\alpha' \varepsilon_0 \sigma_0 I_n} \right)^{n/(n+1)} r^{1/(n+1)} \tilde{u}(\pi), \quad [5]$$

where δ is the crack opening displacement (COD), ε_0 , n , and a_0 are the constants in the constitutive equation for a power-law hardening material, J is the J -integral, σ_0 is the flow stress, r is the distance behind a crack tip, I_n is an integral constant, and $\tilde{u}(\pi)$ is the value of a dimensionless normalization function at $\theta = \pi$. The J -integral was calculated based on Eq. [6] from the

CTOD, δ , experimentally measured from the virtual cross section of the cracks (slices A, B, and C in Figures 12 and 13).

$$J = \frac{\sigma_0 \delta}{d_n}, \quad [6]$$

where d_n is a dimensionless constant. The stress and strain in the crack tip region have a singularity of $r^{1/(n+1)}$ in this HRR solution. The RDS solution is expressed as follows:

$$\frac{E\delta}{\sigma_0 r} = \alpha T_R + \beta \ln \left(\frac{e R_p}{r} \right), \quad [7]$$

where E is Young's modulus, T_R is the material tearing modulus, e is Napier's constant, and R_p is the plastic zone diameter. T_R was calculated as follows^[64]:

$$T_R = \frac{\Omega}{3\alpha} - \frac{\beta}{\alpha} \ln \left(\frac{e\lambda\Omega}{3\alpha} \right)$$

with

$$\Omega = \frac{E\varepsilon_f}{\sigma_0}, \quad [8]$$

where α , β , and λ are constants and were assumed to be 0.65, 5.08, and 0.2 respectively.^[64] The calculated T_R values were 12.5 and 8.7 for intergranular cracks and quasi-cleavage cracks, respectively. According to Chan *et al.*, these calculated T_R values are classified as being within the "brittle fracture regime."^[64] The RDS solution shown in Eq. [7] is derived from the exact solution based on strain increment theory, and it shows a weak singularity proportional to $\ln(1/r)$. For the purpose of experimental evaluation of the above singularities, it is extremely challenging to measure the stress and strain in the local region of the crack tip inside the material. However, the singularity of the crack tip region can be evaluated by measuring the COD along the crack surface and comparing the value of δ derived from the HRR and RDS solutions. In addition, Toda *et al.* analyzed the transition of the singularity from HRR to RDS due to crack growth in three dimensions by using the COD profile directly measured by tomographic observation.^[61]

In this study, the displacement fields (*i.e.*, local deformation region) of the intergranular and quasi-cleavage crack tip regions were analyzed in terms of the abovementioned singularities. The HRR and RDS singularities based on Eqs. [5] and [7] are applicable when the stress/strain field at the crack tip is a K -dominated or J -dominated region. The analysis based on Eqs. [5] and [7] cannot be applied if the stress/strain field at the crack-tip exhibits large-scale yielding. As shown in Figures 11 through 15, the microcracks observed in this study were mostly 3D microcracks embedded in an elastic-plastic field. If large-scale yielding occurs at the crack tip, the measured CTOD corresponding to the size of the process zone at the crack tip would be large. As shown in Figure 15, the CTODs of intergranular cracks and quasi-cleavage cracks were small, at most approximately 1 μm . At the

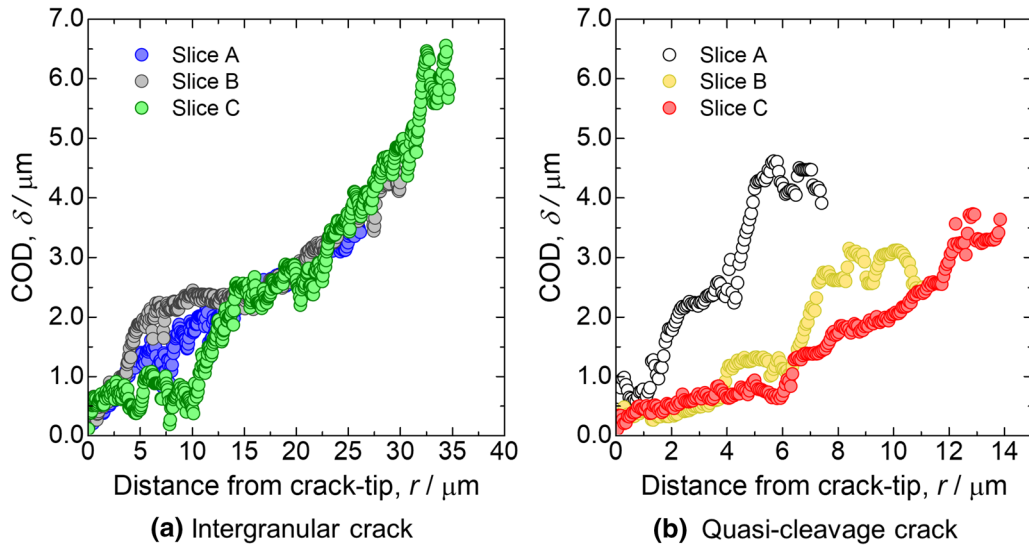


Fig. 16—Variation of the crack opening displacement from the crack tip, which was obtained from slices A, B, and C in Figs. 12 and 13. (a) and (b) correspond to intergranular and quasi-cleavage cracks, respectively (Color figure online).

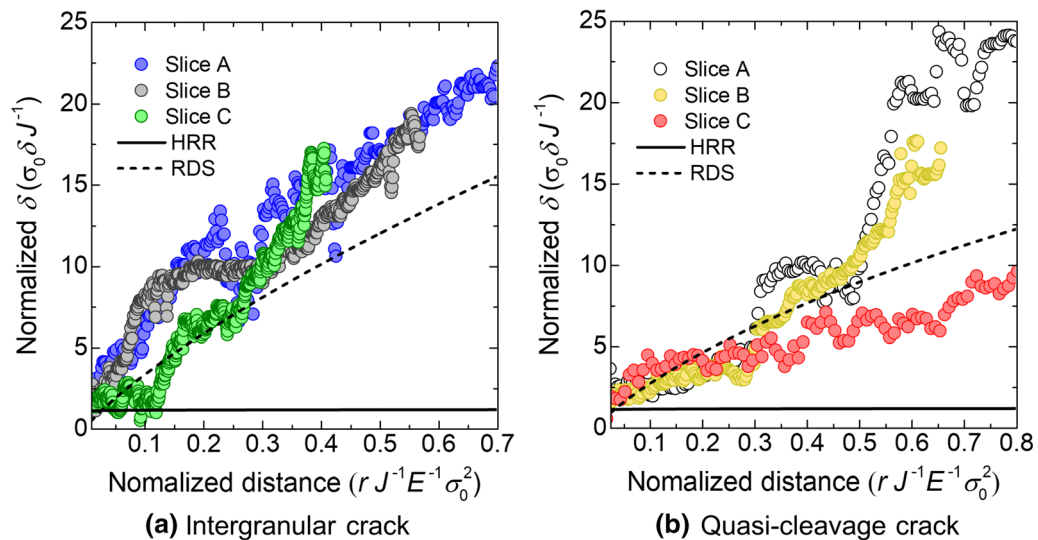


Fig. 17—Normalized crack opening profile as a function of normalized distance for the (a) intergranular and (b) quasi-cleavage crack tips (Color figure online).

tip of such a crack, it is unlikely that large-scale yielding has occurred. Thus, in the following discussion, it was rationally assumed that their crack tips were K -dominated or J -dominated regions.

The COD profiles obtained from Figures 12(c) through (e) and 13(c) through (e) are shown in Figures 16(a) and (b), respectively. The kink in the COD profile, which is presumed to be due to propagation of the adjacent grain boundary, was observed in the intergranular crack. Relative to an intergranular crack, the COD profiles of a quasi-cleavage crack vary frequently, which corresponds to facet structure on the fracture surface. Figure 17 shows normalized COD profiles that were experimentally obtained from COD profiles in Figure 16 and normalized COD profiles generated by the HRR and RDS solutions. Here, to

compare the two solutions expressed as Eqs. [5] and [7], the distance from the crack tip, r , and the COD, δ , were normalized using the J -integral, flow stress, and Young's modulus. As a result, the stress and strain fields in both crack tip regions do not follow the HRR solution; they follow the RDS solution only in the quite limited range of the crack tip. The regions following the RDS solution in the intergranular crack and the quasi-cleavage cracks were the regions where the normalized distance is equal to 0.2-0.3 (*i.e.*, 15-20 μm from the crack tip) and 0.2 or less (*i.e.*, 0.6-5 μm from crack tip), respectively. The RDS solution means that elastic unloading occurs above and below the crack surface when a sharp crack propagates into the plastic zone and that the stress and strain singularity in the crack tip region weaken in proportion to $\ln(1/r)$. The analysis shown in Figure 17

suggests that strain has already been localized prior to crack initiation and that sharp cracks grow toward the strain-localized region. This important finding is consistent with the strain mapping ahead of the quasi-cleavage crack shown in Figure 11(b). Since the region following the RDS solution is within 5 μm of the crack tip, it can be concluded that the localization of the strain at the crack tip does not appear in the strain mapping of Figure 11(b). The region following the RDS solution of the intergranular crack is slightly larger than the quasi-cleavage crack and lies 15 to 20 μm from the crack tip. This result reveals the effect of heterogeneous deformation near the grain boundary, as the Al-10.1Zn-1.2 Mg alloy used had a coarse grain of approximately 330 μm , which imparts a loose plastic constraint from adjacent grains. In addition, the alloy has a coarse precipitate and a precipitate-free zone on the grain boundaries.^[65] Thus, in both intergranular and quasi-cleavage cracks, the local deformation, which follows the RDS solution, was quantitatively revealed in the region of 20 μm or less from the crack tip. Local plastic deformation occurs at the crack tip, and its plastic zone size is significantly more limited than that of a typical ductile crack.

V. CONCLUSION

The HE behaviors of Al-10.1Zn-1.2 Mg alloy and Al-9.9Zn-2.3Mg-1.4Cu alloy were analyzed by means of *in situ* observation using synchrotron projection-type and imaging-type tomography. Similar to the already reported behavior of the Al-9.9Zn-2.3Mg-1.4Cu alloy, HE appeared significant when the holding time of the *in situ* test increased, and the area fractions of intergranular and quasi-cleavage fractures increased. However, the fractures were not completely brittle, and even the intergranular crack that grew on one grain boundary did not grow in a single step but instead grew progressively by tensile loading. When trace iron was added to the Al-10.1Zn-1.2Mg alloy, the area fractions of intergranular and quasi-cleavage fractures decreased, and HE was suppressed even if the hydrogen content of the material was approximately the same. Based on the TDA results, it was concluded that the hydrogen contents in trap sites such as dislocation and grain boundaries decreased relatively and that HE was suppressed because the second-phase particles trapped hydrogen. In addition, it was found that these HE behaviors are dominated by hydrogen in the matrix and that pores filled with molecular hydrogen do not directly affect HE. The contribution of the plastic deformation to intergranular and quasi-cleavage crack growth has been examined in this study. 3D strain mapping could not visualize their strain fields because their sizes are smaller than 18 μm , and the RDS solution also suggests that the local deformation regions of the crack tip were quite limited. Furthermore, intergranular cracks grown at fixed displacement were visualized in the specimen with the extremely increased hydrogen content, and the crack driving force was attributed to hydrogen accumulation.

ACKNOWLEDGMENTS

This research was supported by the Japan Science and Technology Agency (JST) under Collaborative Research Based on Industrial Demand “Heterogeneous Structure Control: Towards Innovative Development of Metallic Structural Materials.” This research was supported in part by a grant from the Light Metal Educational Foundation, Japan. The synchrotron radiation experiments were performed at the BL20XU and the BL37XU of SPring-8 with the approval of the Japan Synchrotron Radiation Research Institute (JASRI) (Proposal Nos. 2016A1199, 2016B1081, 2016A0076, 2016B0076). The authors also thank Dr. Takahiro Shikama in KOBELCO and the Japan Aluminium Association for providing and preparing the materials used.

REFERENCES

1. R.G. Song, W. Dietzel, B.J. Zhang, W.J. Liu, M.K. Tseng, and A. Atrens: *Acta Mater.*, 2004, vol. 52, pp. 4727–43.
2. M.S. Bhuiyan, H. Toda, Z. Peng, S. Hang, K. Horikawa, K. Uesugi, A. Takeuchi, N. Sakaguchi, and Y. Watanabe: *Mater. Sci. Eng. A*, 2016, vol. 655, pp. 221–28.
3. M. Hirano, K. Kobayashi, and H. Tonda: *J. Soc. Mater. Sci. Japan*, 2000, vol. 49, pp. 86–91.
4. R. Braun: *Materwiss. Werksttech.*, 2007, vol. 38, pp. 674–89.
5. D. Najjar, T. Magnin, and T.J. Warner: *Influence of Critical Surface Defects and Localized Competition between Anodic Dissolution and Hydrogen Effects during Stress Corrosion Cracking of a 7050 Aluminium Alloy*, vol. 238, 1997.
6. S. Osaki and S. Haruyama: *J. Japan Inst. Light Met.*, 2013, vol. 63, pp. 57–64.
7. S. Osaki, J. Ikeda, K. Kinoshita, Y. Sasaki, and A.M. Si: *J. Japan Inst. Light Met.*, 2006, vol. 56, pp. 721–27.
8. S. Kuramoto, J. Okahana, and M. Kanno: *Mater. Trans.*, 2001, vol. 42, pp. 42.
9. M.S. Bhuiyan, Y. Tada, H. Toda, S. Hang, K. Uesugi, A. Takeuchi, N. Sakaguchi, and Y. Watanabe: *Int. J. Fract.*, 2016, vol. 200, pp. 13–29.
10. M. Wang, E. Akiyama, and K. Tsuzaki: *Mater. Sci. Eng. A*, 2005, vol. 398, pp. 37–46.
11. K. Takai and R. Watanuki: *ISIJ Int.*, 2003, vol. 43, pp. 520–26.
12. H. Su, H. Toda, R. Masunaga, K. Shimizu, H. Gao, K. Sasaki, M.S. Bhuiyan, K. Uesugi, A. Takeuchi, and Y. Watanabe: *Acta Mater.*, 2018, vol. 159, pp. 332–43.
13. R.A. Oriani: *Acta Metall.*, 1970, vol. 18, pp. 147–57.
14. H. Toda, T. Hidaka, M. Kobayashi, K. Uesugi, A. Takeuchi, and K. Horikawa: *Acta Mater.*, 2009, vol. 57, pp. 2277–90.
15. M. Felberbaum and M. Rappaz: *Acta Mater.*, 2011, vol. 59, pp. 6849–60.
16. P.D. Lee and J.D. Hunt: *Acta Mater.*, 2001, vol. 49, pp. 1383–98.
17. H. Toda, H. Oogo, K. Horikawa, K. Uesugi, A. Takeuchi, Y. Suzuki, M. Nakazawa, Y. Aoki, and M. Kobayashi: *Metall. Mater. Trans. A*, 2014, vol. 45A, pp. 765–76.
18. W.Y. Choo and J.Y. Lee: *Metall. Trans. A*, 1982, vol. 13A, pp. 135–40.
19. P. Chao and R.A. Karnesky: *Mater. Sci. Eng. A*, 2016, vol. 658, pp. 422–28.
20. S.W. Smith and J.R. Scully: *Metall. Mater. Trans. A*, 2000, vol. 31A, pp. 179–93.
21. T. Enomoto, R. Matsumoto, S. Taketomi, and N. Miyazaki: *Zair. Soc. Mater. Sci. Jpn.*, 2010, vol. 59, pp. 596–603.
22. K. Horikawa and K. Yoshida: *Mater. Trans.*, 2004, vol. 45, pp. 315–18.
23. K. Horikawa, H. Okada, H. Kobayashi, and W. Urushihara: *Mater. Trans.*, 2009, vol. 50, pp. 759–64.
24. H. Matsunaga, T. Usuda, K. Yanase, and M. Endo: *Metall. Mater. Trans. A*, 2014, vol. 45A, pp. 1315–26.

25. T. Izumi and G. Itoh: *Mater. Sci. Forum*, 2007, vols. 539–543, pp. 475–80.
26. K. Ichitani, M. Kanno, and S. Kuramoto: *ISIJ Int.*, 2003, vol. 43, pp. 496–504.
27. I.M. Robertson, P. Sofronis, A. Nagao, M.L. Martin, S. Wang, D.W. Gross, and K.E. Nygren: *Metall. Mater. Trans. A*, 2015, vol. 46A, pp. 2323–41.
28. M. Yamaguchi, K.I. Ebihara, M. Itakura, T. Kadoyoshi, T. Suzudo, and H. Kaburaki: *Metallurgical and Materials Transactions A: Physical Metallurgy and Materials Science*, Springer, US, 2011, vol. 42, pp. 330–39.
29. M. Yamaguchi, J. Kameda, K.-I. Ebihara, M. Itakura, and H. Kaburaki: *Philos. Mag.*, 2012, vol. 92, pp. 1349–68.
30. Y. Mine, T. Tsumagari, and Z. Horita: *Scr. Mater.*, 2010, vol. 63, pp. 552–55.
31. M. Nagumo: *Mater. Sci. Technol.*, 2004, vol. 20, pp. 940–50.
32. T. Neeraj, R. Srinivasan, and J. Li: *Acta Mater.*, 2012, vol. 60, pp. 5160–71.
33. M.L. Martin, J.A. Fenske, G.S. Liu, P. Sofronis, and I.M. Robertson: *Acta Mater.*, 2011, vol. 59, pp. 1601–06.
34. H. Toda, K. Shimizu, K. Uesugi, Y. Suzuki, and M. Kobayashi: *Mater. Trans.*, 2010, vol. 51, pp. 2045–48.
35. M. Kobayashi, H. Toda, Y. Kawai, T. Ohgaki, K. Uesugi, D.S. Wilkinson, T. Kobayashi, Y. Aoki, and M. Nakazawa: *Acta Mater.*, 2008, vol. 56, pp. 2167–81.
36. H. Su, T. Yoshimura, H. Toda, M.S. Bhuiyan, K. Uesugi, A. Takeuchi, N. Sakaguchi, and Y. Watanabe: *Metall. Mater. Trans. A*, 2016, vol. 47A, pp. 6077–89.
37. T. Ishikawa and R.B. McLellan: *Acta Metall.*, 1986, vol. 34, pp. 1091–95.
38. Japan Institute of Light Metals, ed.: *Structures and Properties of Aluminum*, Tokyo, 1991.
39. J.R. Scully, G.A. Young, and S.W. Smith: in *Gaseous Hydrogen Embrittlement of Materials in Energy Technologies: The Problem, its Characterisation and Effects on Particular Alloy Classes*, Woodhead Publishing, 2012, pp. 707–68.
40. M. Yamaguchi, T. Tsuru, K. Ebihara, and M. Itakura: *J. Jpn. Inst. Light Met.*, 2018, vol. 68, pp. 588–95.
41. A. Takeuchi, K. Uesugi, Y. Suzuki, S. Itabashi, and M. Oda: *J. Synchrotron Rad.*, 2017, vol. 24, pp. 586–94.
42. A. Takeuchi, K. Uesugi, and Y. Suzuki: *J. Phys. Conf. Ser.*, 2017, vol. 849, p. 012055.
43. H. Toda, S. Yamamoto, M. Kobayashi, K. Uesugi, and H. Zhang: *Acta Mater.*, 2008, vol. 56, pp. 6027–39.
44. W.E. Lorensen, H.E. Cline, W.E. Lorensen, and H.E. Cline: in *Proceedings of the 14th annual conference on Computer graphics and interactive techniques - SIGGRAPH '87*, vol. 21, ACM Press, New York, New York, USA, 1987, pp. 163–9.
45. M. Yamaguchi, K.-I. Ebihara, M. Itakura, T. Tsuru, K. Matsuda, and H. Toda: *Comput. Mater. Sci.*, 2019, vol. 156, pp. 368–75.
46. H. Toda, P.C.C. Qu, S. Ito, K. Shimizu, K. Uesugi, A. Takeuchi, Y. Suzuki, and M. Kobayashi: *Int. J. Cast Met. Res.*, 2014, vol. 27, pp. 369–77.
47. P.N. Anyalebechi: *Cast Met.*, 2016, vol. 3, pp. 182–201.
48. M.S.I.T. MSIT®: in *Light Metal Systems. Part 3*, Springer-Verlag, Berlin/Heidelberg, pp. 1–21.
49. T. Izumi and G. Itoh: *Mater. Trans.*, 2011, vol. 52, pp. 130–34.
50. G.A. Young and J.R. Scully: *Acta Mater.*, 1998, vol. 46, pp. 6337–49.
51. H. Toda, Z.A.B. Shamsudin, K. Shimizu, K. Uesugi, A. Takeuchi, Y. Suzuki, M. Nakazawa, Y. Aoki, and M. Kobayashi: *Acta Mater.*, 2013, vol. 61, pp. 2403–13.
52. Y.S. Chen, D. Haley, S.S.A. Gerstl, A.J. London, F. Sweeney, R.A. Wepf, W.M. Rainforth, P.A.J. Bagot, and M.P. Moody: *Science*, 2017, vol. 355, pp. 1196–99.
53. J. Takahashi, K. Kawakami, and Y. Kobayashi: *Acta Mater.*, 2018, vol. 153, pp. 193–204.
54. H. Saitoh, Y. Iijima, and K. Hirano: *J. Mater. Sci.*, 1994, vol. 29, pp. 5739–44.
55. F.G. Wei, T. Hara, and K. Tsuzaki: *Metall. Mater. Trans. B*, 2004, vol. 35B, pp. 587–97.
56. D. Nguyen, A.W. Thompson, and I.M. Bernstein: *Acta Metall.*, 1987, vol. 35, pp. 2417–25.
57. H. Gao, H. Su, K. Shimizu, C. Kadokawa, H. Toda, Y. Terada, K. Uesugi, and A. Takeuchi: *Mater. Trans.*, 2018, vol. 59, pp. 1532–35.
58. T. Tsuru, M. Yamaguchi, H. Toda, and K. Shimizu: unpublished work.
59. P. Sofronis and R.M. McMeeking: *J. Mech. Phys. Solids*, 1989, vol. 37, pp. 317–50.
60. K. Hirayama, Y. Sek, T. Suzuki, H. Toda, K. Uesugi, A. Takeuchi, and W. Ludwig: in preparation.
61. H. Toda, E. Maire, S. Yamauchi, H. Tsuruta, T. Hiramatsu, and M. Kobayashi: *Acta Mater.*, 2011, vol. 59, pp. 1995–2008.
62. J.R. Rice, W.J. Drugan, and T.L. Sham: *ASTM STP*, 1980, vol. 700, pp. 189–221.
63. K.S. Chan: *Metall. Trans. A*, 1990, vol. 21A, pp. 81–86.
64. K.S. Chan: *Acta Metall.*, 1989, vol. 37, pp. 1217–26.
65. T. Ogura, T. Otani, A. Hirose, and T. Sato: *Mater. Sci. Eng. A*, 2013, vol. 580, pp. 288–93.

Publisher's Note Springer Nature remains neutral with regard to jurisdictional claims in published maps and institutional affiliations.